An analytical model of sound refraction by the fuselage boundary-layer for fan tone radiation from a turbofan aero-engine*

Dionysios-Marios Rouvas† and Alan McAlpine‡
Institute of Sound and Vibration Research, University of Southampton, Southampton, SO17 1BJ, United Kingdom

The work presented in this paper is on the development and validation of an analytical-based model to predict scattering of fan tone noise from a turbofan engine by the airframe fuselage and refraction due to the presence of a boundary layer on the fuselage. The aim is to avoid numerical solutions to calculate sound propagation through the fuselage boundary layer which have been prevalent in previous work on this topic. The work presented here is a continuation of the work by the authors in which the 1/7th power-law boundary-layer velocity profile was replaced with a linear profile which enabled an analytical solution of the Pridmore-Brown equation. The work presented here offers an even simpler alternative solution by replacing the power-law profile with a step function. This approach once again leads to a far-field solution in terms of a Fourier series, and a near-field solution expressed in terms of a Fourier series and an inverse Fourier transform. The two approaches utilising a linear or step-function velocity profile are compared with each other, and against existing numerical results. The results show that for sufficiently thin boundary-layers both approaches can approximate a more realistic power-law boundary-layer profile, while the accuracy of the step-function solution appears to not deteriorate with thicker layers. A parametric study based on multi-modal simulations is performed with realistic operating and flight conditions. Predictions for boundary-layer shielding and the far-field polar directivity are generated with both linear and step-function profiles, and there is reasonable agreement comparing results for the two velocity profiles.

I. Nomenclature

a	=	duct radius, m
a_0	=	fuselage radius, m
b	=	distance between the centreline of the fuselage and centreline of the intake duct, m
c_0	=	speed of sound, m·s^{-1}
D_n	=	coefficient for the step-function boundary layer expressions
$\mathrm{H}_m^{(2)}$	=	Hankel function of the second kind, order m
I	=	denotes an integral
J_m	=	Bessel function of the first kind, order m
K	=	non-dimensional axial wavenumber
k_0	=	freespace wavenumber, rad·m^{-1}
k_{zlq}	=	axial wavenumber, mode (l, q), rad·m^{-1}
l	=	azimuthal order
M_∞	=	free-stream Mach number
M_w	=	Mach number at the fuselage surface

*This is the author's version (post-print) of the work that was accepted for publication in the proceedings of the 28th AIAA/CEAS Aeroacoustics Conference, June 14-17, 2022.

The final version was published in the proceedings of the conference as paper No. 2022-3059. https://doi.org/10.2514/6.2022-3059

†PhD Candidate, Institute of Sound and Vibration Research (ISVR), dmr1e18@soton.ac.uk.
‡Associate Professor, Institute of Sound and Vibration Research (ISVR), A.McAlpine@soton.ac.uk.

P_{lq} = pressure amplitude of mode (l, q), Pa
p' = acoustic pressure, Pa
q = radial order
(r, ϕ, z) = cylindrical coordinate system centered on the intake duct (or disc source)
$(\bar{r}, \bar{\phi}, \bar{z})$ = cylindrical coordinate system centered on the fuselage
$(\bar{R}, \bar{\theta}, \bar{\phi})$ = spherical polar coordinate system centred on the fuselage
t = time, s
W_{lq} = sound power of mode (l, q), Watt
W_t = total sound power of source, Watt
Γ = radial wavenumber, rad·m^{-1}
γ = alternative form of radial wavenumber, rad·m^{-1}
Δ_0 = wavenumber in real space used in far-field analysis, dependent on $\bar{\theta}$, rad·m^{-1}
Δ_{bl} = difference between sound pressure level with and without the presence of a boundary layer, dB
Δ_{source} = difference between sound pressure level due to different sources
δ = boundary layer thickness, m
ϵ = non-dimensional error metric
ε = non-dimensional boundary-layer thickness
ζ = non-dimensional radial coordinate used to denote location within the boundary layer
κ_{lq} = modal eigenvalue, mode (l, q), rad·m^{-1}
φ = Mach number distribution inside the boundary layer, dependent on ζ
ω_0 = angular frequency, rad·s^{-1}

Subscripts

ff = denotes far-field quantity
i = denotes incident field
in = denotes field inside the linear boundary layer
n = denotes quantity is a Fourier–Bessel harmonic
∞ = denotes field outside the boundary layer or free-stream value
s = denotes scattered field
t = denotes total field
0 = denotes field inside the step-function boundary layer

Superscripts

$'$ = denotes differentiation with respect to a function's argument
ee = denotes source with equal energy per mode
20 = denotes rotor-locked source with dominant mode's sound power 20 dB higher than all other cut-on modes
30 = denotes rotor-locked source with dominant mode's sound power 30 dB higher than all other cut-on modes

Symbol

$\widehat{\ }$ = denotes time-harmonic quantity
$\bar{\ }$ = denotes Fourier transformed quantity

II. Introduction

Since the introduction of the turbojet engine seventy years ago, understanding and predicting the generation of aircraft noise has inspired the work of many researchers. This is evident when one considers that organisations such as the International Civil Aviation Organisation [1], and the American Federal Aviation Administration, have introduced rules and regulations that dictate certain standards regarding noise produced by aircraft. In order for the aircraft manufacturing

industry to meet those standards and keep the noise pollution at the required minimum, while the frequency of flights keeps on increasing, a variety of accurate noise prediction methods are used. Currently, these approaches are principally numerical-based methods. The purpose of the work presented in this paper is to provide an alternative theoretical method that solves a simplified problem producing results in a far shorter amount of time.

Generally, in the field of aeroacoustics, the noise sources on the aircraft can be categorised into three broad groups as explained. These are engine noise, jet noise and airframe noise. However, the intensity of each of these sources is dependent on the configuration of the aircraft, such as the shape and dimensions of the fuselage and the wings, the position of the engines, and the flight conditions. Fan noise is dominant both during take-off and approach. However, when one considers the work of Hanson [2], Hanson and Magliozzi [3], Fuller [4], Gaffney et al. [5] and Rouvas & McAlpine [6], it is apparent that predicting the propagation of fan noise radiated from the nacelle into free space is not sufficiently accurate since the turbofan is installed on the airframe. The noise produced by the engine will interact with the fuselage and the wings of the aircraft which will alter the resulting sound field. These interactions are called acoustic installation effects.

As explained in Rouvas & McAlpine [6], in recent years research on installation effects has been focused on fan noise due to the popularity of the turbofan engine and its dominance over jet noise which has been diminished with the development of high-bypass turbofan engines. It is therefore of utmost importance for the industry to have tools that will generate quick trends regarding installation effects of fan noise, since the Effective Perceived Noise Level (EPNL) metric and community noise exposure is a function of noise generated by the aircraft as a whole. It is also important to point out that alterations are expected both in the near and the far field, further highlighting the benefit of calculating the installed sound field instead of the free-field response of the noise source.

Most of the research on fuselage scattering involves the effect of refraction due to the presence of a boundary layer along the fuselage as illustrated in Fig. (1). Sound is expected to refract away from the fuselage upstream of the source. That characteristic effect has been investigated before and it has proven to play a major role that cannot be ignored. McAninch [7] was the first researcher to investigate this effect and the first to point out the difficulties involved in solving the problem of sound propagating through a shear flow. Tam and Morris [8] proposed a method to bridge the singularity apparent in the Pridmore-Brown equation [9], which is the equation governing the problem. The method proposed by Tam and Morris [8] facilitated the use of numerical schemes to solve the equation, as shown by Hanson and Magliozzi [3], Gaffney et al [5], Lu [11], Belyaev [12] and Brouwer [13]. The last three even extended the methods to derive far-field results, in contrast with the other researchers whose studies were limited to the near-field and specifically prediction of the acoustic pressure on the fuselage surface.

Hanson and Magliozzi [3] were the first to develop a model that could predict the total acoustic field on the fuselage surface due to scattering and refraction of a propeller noise source. Propeller noise sources were used in most of the previous prediction models (e.g. [4], [11], [12], [13]), until recently with the introduction of fan noise sources by McAlpine et al. [16] and Gaffney et al [5]. They used a distributed disc source to model a spinning mode exiting a fan duct. It is important to note that all these studies utilised high-fidelity numerical schemes to solve the Pridmore-Brown equation, namely Runge–Kutta routines which prove to be very time-consuming. There have been attempts to solve the problem analytically with asymptotic methods used mainly in duct acoustics by Eversman and Beckemeyer [14] and Goldstein and Rice [15]. The work by Rouvas and McAlpine [6] uses these asymptotic methods to construct a model for prediction of fan noise scattering and refraction effects, a model that is extended and improved in the present paper.

The work in this paper is a direct continuation of the work presented in Rouvas & McAlpine [6]. The reflection and diffraction of fan tone noise by the fuselage was the primary research aim in Ref. [6]. Since fan noise includes strong tonal components, the analysis was based on time-harmonic spinning modes exiting a cylindrical duct and impinging on an adjacent cylidrical fuselage. The key aim was to derive analytic expressions that describe the acoustic near- and far-field from an installed fan noise source adjacent to a cylindrical fuselage as shown in Fig. (2). This configuration replicates the real-life situation of an engine located adjacent to the fuselage when mounted under the wing. The fan noise source was modelled as a distribution of monopoles on a disc, simulating a spinning mode. Rouvas and McAlpine investigated the reflection and diffraction of the sound field by the fuselage, but also a lot of focus was given to the refraction effect owing to the presence of a boundary layer along the fuselage, as illustrated in Fig. (2) with thickness δ.

The key contribution in Rouvas & McAlpine [6] was the derivation of an analytic expression to solve the problem of sound propagation through a shear layer which previously had been carried out using high-fidelity numerical methods. In order to achieve that, a simpler linear velocity profile was modelled. Rouvas & McAlpine employed an asymptotic approach outlined in Eversman and Beckemeyer [14], which is valid for sufficiently thin boundary layers. They proved that the asymptotic approach was able to simulate the refraction effect of a realistic turbulent boundary layer, especially when the layer is sufficiently thin compared to the fuselage radius and the wavelength, and it was implied that even

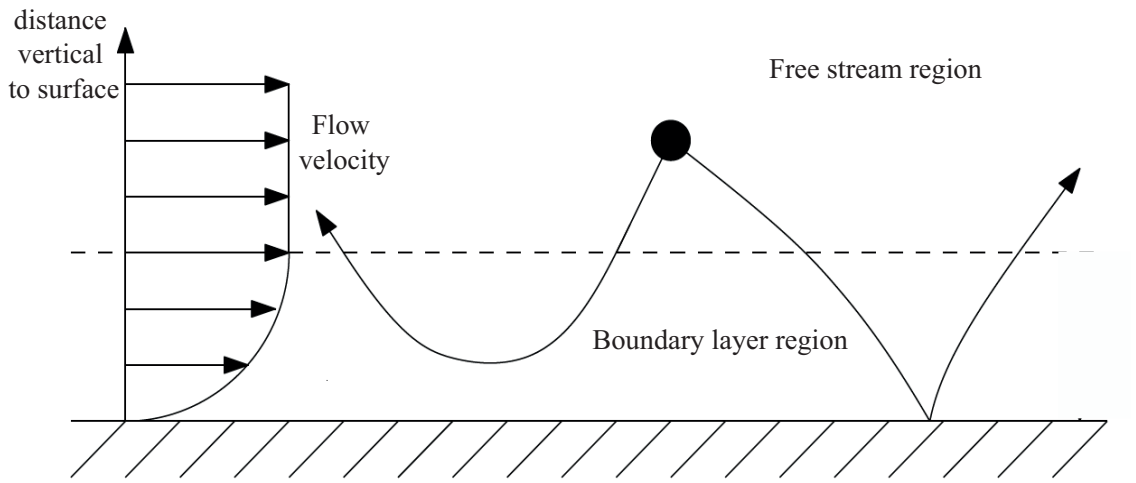

Fig. 1 Sketch of refracted rays downstream and upstream of the source. Taken from [17].

simpler profiles could be used instead of the linear one.

This investigation is the main scope of this paper, which simplifies the velocity profile to its most rudimentary form: a step-function profile [2]. The analysis follows the same methodology as in the linear profile approach outlined in [6]. Analytic expressions are derived for the far-field in terms of a Fourier series and the near-field in terms of a Fourier series and an inverse Fourier transform integral. The derived expressions are validated by comparing against existing numerical solutions. The advantage of the step-function approach lies in the fact that it does not require the solution of the Pridmore-Brown equation [9] reducing the complexity of the problem and the need for high-fidelity numerical schemes. The entire formulation is based on solving only the convected wave equation.

The second objective of this paper is to compare the two approaches (linear or step-function velocity profile), and assess their effectiveness in approximating the shielding effect of a 1/7th power-law profile that is representative of a realistic turbulent boundary-layer. This involves an investigation into which is the optimal method to use, by matching the equivalent simplified velocity profiles to the power-law profile. Some preliminary work on this has already been reported by Rouvas & McAlpine [10], and is discussed in more depth in this article. The expressions and equations derived in this article are validated by demonstrating that very similar results can be generated compared to results that use numerical schemes to solve the sound propagation through a 1/7th power-law boundary-layer profile.

Thirdly, another objective of this paper is to use the analytical methods for a parametric study that incorporates realistic aircraft dimensions, configurations and flight conditions. A generic test model is created that represents a wide-body aircraft that is typically equipped with a high-bypass-ratio turbofan engine and typical flight conditions are assumed. The ultimate objective of this study is to provide a more cost-effective prediction tool as an alternative to more common high-fidelity numerical schemes.

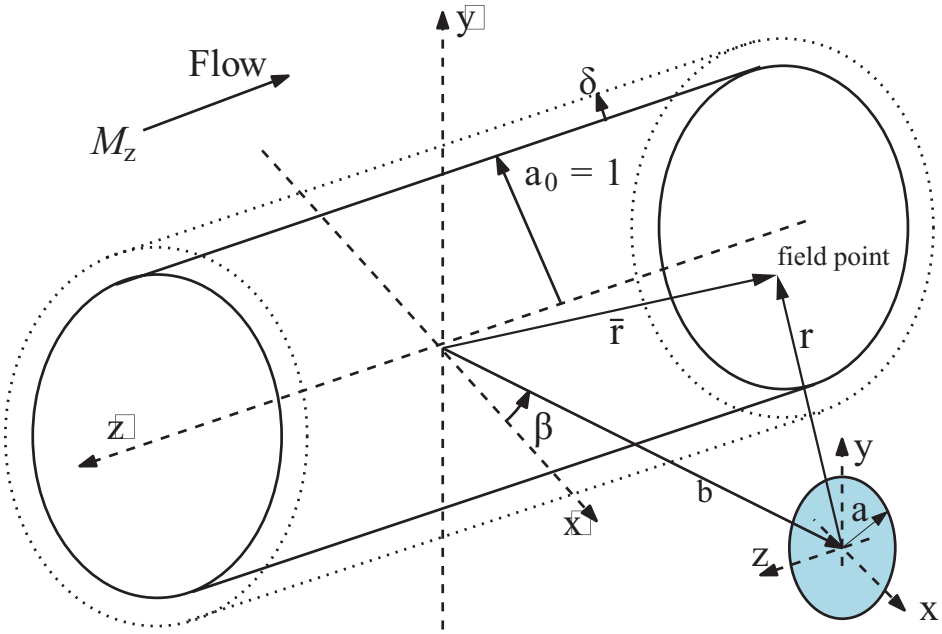

Fig. 2 Sketch of the cylindrical fuselage with radius a_0 adjacent to the disc source with radius a. The centerlines of the fuselage and the source are aligned and have distance b between them. On the fuselage there is a boundary layer with thickness δ. Taken from [5].

III. Theoretical Background and Analysis

A. Uniform Flow

Following McAlpine, Gaffney & Kingan [16], and Rouvas & McAlpine [6], the analysis starts by considering a ducted fan in a cylindrical intake of radius a. The original Cartesian coordinate system (x, y, z) that is used has its z-axis coincident with the centreline of the intake duct (as shown in Fig. (2)). Also there is a subsonic uniform mean flow, with Mach number $M_z = U_z/c_0$, directed in the negative z-direction. The sound field generated by the ducted fan is modelled using "spinning modes" [18]. To avoid any confusion, it is stated that in the following analysis the time-harmonic convention is $\exp\{+\mathrm{i}\omega_0 t\}$. A time-harmonic spinning mode with azimuthal order l and radial order q has acoustic pressure and axial particle velocity given by eqs.(1)–(4) from [16]

$$\hat{p}_{lq} = P_{lq} \mathrm{J}_l(\kappa_{lq} r) \mathrm{e}^{\mathrm{i}(-l\phi - k_{zlq} z)}, \tag{1}$$

$$\hat{u}_{zlq} = \frac{\xi_{lq}}{\rho_0 c_0} P_{lq} \mathrm{J}_l(\kappa_{lq} r) \mathrm{e}^{\mathrm{i}(-l\phi - k_{zlq} z)}, \tag{2}$$

where P_{lq} is the modal amplitude, and

$$\xi_{lq} = \frac{k_{zlq}}{(k_0 + k_{zlq} M_z)}, \tag{3}$$

with dispersion relationship given by

$$k_{zlq}^2 + \kappa_{lq}^2 = (k_0 + k_{zlq} M_z)^2. \tag{4}$$

The Bessel function of the first kind and order l is denoted by J_l. Also, κ_{lq} is the set of eigenvalues which satisfy $\mathrm{J}_l'(\kappa_{lq} a) = 0$, k_{zlq} is the axial wavenumber of mode (l, q), c_0 is the speed of sound, ρ_0 is the mean density of the air inside the duct, and $k_0 = \omega_0/c_0$. The acoustic field is expressed in cylindrical polar coordinates (r, ϕ, z) where $x = r\cos\phi$ and $y = r\sin\phi$.

From McAlpine et al. [16], the acoustic pressure generated by a fan tone exiting a duct can be modelled by integrating a distribution of monopole sources over the cross-section of the duct termination. The derivation of the

incident field is described in [16] and briefly in the appendix of Ref. [6]. In this article, the theoretical formulation is omitted and only the key equations are given.

The governing equation is the inhomogeneous convected wave equation, which is solved by first transforming to the Fourier frequency-wavenumber domain. The solution in free space is referred to as the incident field. The coordinate system is shifted from the duct centerline (x, y, z) to the fuselage centerline $(\bar{x}, \bar{y}, \bar{z})$, as shown in Fig. (2), using Graf's Addition Theorem listed in Abramowitz and Stegun [19]. This adjusts the incident field wavenumber spectrum giving a solution that is dependent on $\bar{r}$ instead of r. For the near-field result where $\bar{r} < b$, the Fourier-transformed incident pressure field is dependent on $\bar{r}$ via a Bessel function

$$\overline{p'_{in}}\,(\bar{r}, k_z, t) \;=\; \pi^2 \xi_{lq} P_{lq} (-1)^{l+n} (k_0 + k_z M)\, \Psi_{lq}\, \mathrm{e}^{-\mathrm{i}(l-n)\beta}\, \mathrm{H}^{(2)}_{l-n}\,(\Gamma_0 b)\, \mathrm{J}_n\,(\Gamma_0 \bar{r})\, \mathrm{e}^{\mathrm{i}\omega_0 t}, \tag{5}$$

where $\Gamma_0^2 = (k_0 + k_z M)^2 - k_z^2$ is a radial wavenumber. The function Ψ_{lq} is given by

$$\Psi_{lq} = \frac{\Gamma_0 a}{\kappa_{lq}^2 - \Gamma_0^2} \mathrm{J}_l(\kappa_{lq} a) \mathrm{J}'_l(\Gamma_0 a), \quad \Gamma_0 \neq \kappa_{lq}, \tag{6}$$

$$\Psi_{lq} = \frac{1}{2}\left(a^2 - \frac{l^2}{\kappa_{lq}^2}\right) \mathrm{J}_l^2(\kappa_{lq} a), \quad \Gamma_0 = \kappa_{lq}. \tag{7}$$

McAlpine et al. [16] did not derive the far-field result. In this case, where $\bar{r} >> b$, application of Graf's theorem gives a modified incident field dependent on $\bar{r}$ via a Hankel function (as derived in Ref. [6]),

$$\overline{p'_{in}}\,(\bar{r}, k_z, t) \;=\; \pi^2 \xi_{lq} P_{lq}\, (k_0 + k_z M)\, \Psi_{lq}\, \mathrm{e}^{\mathrm{i}(n-l)\beta}\, \mathrm{J}_{n-l}\,(\Gamma_0 b)\, \mathrm{H}^{(2)}_n\,(\Gamma_0 \bar{r})\, \mathrm{e}^{\mathrm{i}\omega_0 t}. \tag{8}$$

The presence of the cylindrical fuselage causes reflection and diffraction of the incident field. Thus the total field is expressed as the sum of the incident field and a scattered field, where the 'scattering' is caused by the rigid, hard-walled cylinder in the field. The governing equation that describes the scattered field is the homogeneous convected wave equation, and since the solution must be outward propagating cylindrical waves, it can be expressed in terms of Hankel functions. By employing a rigid, hard-walled boundary condition at the cylindrical fuselage surface,

$$\frac{\partial \overline{p'_{tn}}}{\partial \bar{r}} = \frac{\partial \overline{p'_{in}}}{\partial \bar{r}} + \frac{\partial \overline{p'_{sn}}}{\partial \bar{r}} = 0 \quad \text{at} \quad \bar{r} = a_0, \tag{9}$$

where $\overline{p'_{in}}$ is the near-field expression of eq.(5) since the fuselage surface lies in the near-field, the Fourier-transformed scattered field is obtained

$$\begin{aligned} \overline{p'_{sn}}\,(\bar{r}, k_z, t) \;=\; & -\pi^2 \xi_{lq} P_{lq} (-1)^{l+n}\, \mathrm{e}^{-\mathrm{i}(l-n)\beta}\, (k_0 + k_z M)\, \Psi_{lq}\, \mathrm{H}^{(2)}_{l-n}(\Gamma_0 b) \times \\ & \mathrm{H}^{(2)}_n\,(\Gamma_0 \bar{r})\, \frac{\mathrm{J}'_n\,(\Gamma_0 a_0)}{\mathrm{H}^{(2)\prime}_n\,(\Gamma_0 a_0)}\, \mathrm{e}^{\mathrm{i}\omega_0 t}. \end{aligned} \tag{10}$$

Finally the total field is found by summing the incident field and the scattered field, either in the near-field in which case equations (5) and (10) are summed together, or in the far-field in which case equations (8) and (10) are summed together. The total field in real space is found by performing an inverse Fourier z-transform

$$p'_t\,(\bar{r}, \bar{\phi}, \bar{z}, t) \;=\; \frac{1}{(2\pi)^2} \sum_{n=-\infty}^{\infty} \int_{-\infty}^{\infty} \overline{p'_{tn}}\,(\bar{r}, k_z, t)\, \mathrm{e}^{-\mathrm{i}k_z \bar{z}}\, \mathrm{d}k_z\, \mathrm{e}^{-\mathrm{i}n\bar{\phi}}, \tag{11}$$

where $\overline{p'_{tn}}\,(\bar{r}, k_z, t) \;=\; \overline{p'_{in}}\,(\bar{r}, k_z, t) \;+\; \overline{p'_{sn}}\,(\bar{r}, k_z, t)$.

The near-field case, when $\bar{r} = a_0$, describes the pressure on the fuselage surface

$$p'_t\,(a_0, \bar{\phi}, \bar{z}, t) \;=\; \frac{\xi_{lq} P_{lq}}{4}\, (-1)^l\, \mathrm{e}^{-\mathrm{i}l\beta}\, \mathrm{e}^{\mathrm{i}\omega_0 t} \sum_{n=-\infty}^{\infty} \left\{(-1)^n\, \mathrm{e}^{\mathrm{i}n\beta}\, I_n\,(a_0, \bar{z})\, \mathrm{e}^{-\mathrm{i}n\bar{\phi}}\right\}, \tag{12}$$

where

$$I_n\,(a_0, \bar{z}) \;=\; \int_{-\infty}^{\infty} (k_0 + k_z M)\, \Psi_{lq}\, \mathrm{H}^{(2)}_{l-n}\,(\Gamma_0 b) \left[(-\mathrm{i}(2/\pi\Gamma_0 a_0))/\mathrm{H}^{(2)\prime}_n\,(\Gamma_0 a_0)\right] \mathrm{e}^{-\mathrm{i}k_z \bar{z}}\, \mathrm{d}k_z. \tag{13}$$

This integral cannot be solved analytically and a numerical integration routine is employed.

By following the same process but for the far-field case, where equations (8) and (10) are summed together to give an appropriate Fourier-transformed total field $p'_t\,(\bar{r},\bar{\phi},\bar{z},t)$, the inverse Fourier z-transform integral can be solved analytically by employing spherical polar coordinates $(\bar{R},\bar{\theta},\bar{\phi})$, and a large argument approximation for the Hankel function term as outlined in Rouvas & McAlpine [6]. This expresses the integral in an appropriate form to be solved by applying the method of stationary phase, the execution of which can be found in full detail in Ref. [6]. The final far-field expression in terms of spherical polar coordinates is

$$\begin{aligned} p'_{t_{ff}}\,(\bar{R},\bar{\theta},\bar{\phi},t) \;=\; & \frac{\mathrm{i}\xi_{lq}P_{lq}k_0}{2\bar{R}}\,\Psi_{lq}(\Delta_0)\,\frac{S(\bar{\theta})}{(1-M^2\sin^2\bar{\theta})}\,\mathrm{e}^{\mathrm{i}\omega_0 t}\,\mathrm{e}^{-\mathrm{i}k_0\bar{R}S(\bar{\theta})}\sum_{n=-\infty}^{\infty}\mathrm{e}^{\mathrm{i}(n-l)\beta}\,\mathrm{e}^{\frac{1}{2}n\pi\mathrm{i}}\times \\ & \left[\frac{\mathrm{J}_{n-l}\,(\Delta_0 b)\mathrm{H}_n^{(2)\prime}\,(\Delta_0 a_0)-\mathrm{H}_{n-l}^{(2)}\,(\Delta_0 b)\,\mathrm{J}'_n\,(\Delta_0 a_0)}{\mathrm{H}_n^{(2)\prime}\,(\Delta_0 a_0)}\right]\mathrm{e}^{-\mathrm{i}n\bar{\phi}}\,, \end{aligned} \tag{14}$$

where $\Delta_0 = \frac{k_0\sin\bar{\theta}}{(1-M^2\sin^2\bar{\theta})^{1/2}}$ and $S(\bar{\theta}) = \frac{((1-M^2\sin^2\bar{\theta})^{1/2}+M\cos\bar{\theta})}{\sigma^2}$. This far-field expression has been validated by reducing the disc source to a point source, i.e. stationary monopole. This reduces eq. (14) to the known solution for a stationary monopole adjacent to a cylinder given by Bowman et al. (page 127, eq. (2.149), Ref. [20]).

B. Step-Function Boundary-Layer Profile Analysis

The first researcher to propose replacing the actual boundary layer profile by a simplified step-function with effective thickness d was Hanson [2]. The effective thickness d is usually taken to be equal to the displacement thickness or momentum thickness, and thus d is smaller than the actual boundary-layer thickness δ. Inside the step-function boundary-layer, $a_0 < \bar{r} < a_0 + d$, the flow has a Mach number M_0 which is less than the free-stream Mach number M_∞ outside the boundary layer, $\bar{r} > a_0 + d$.

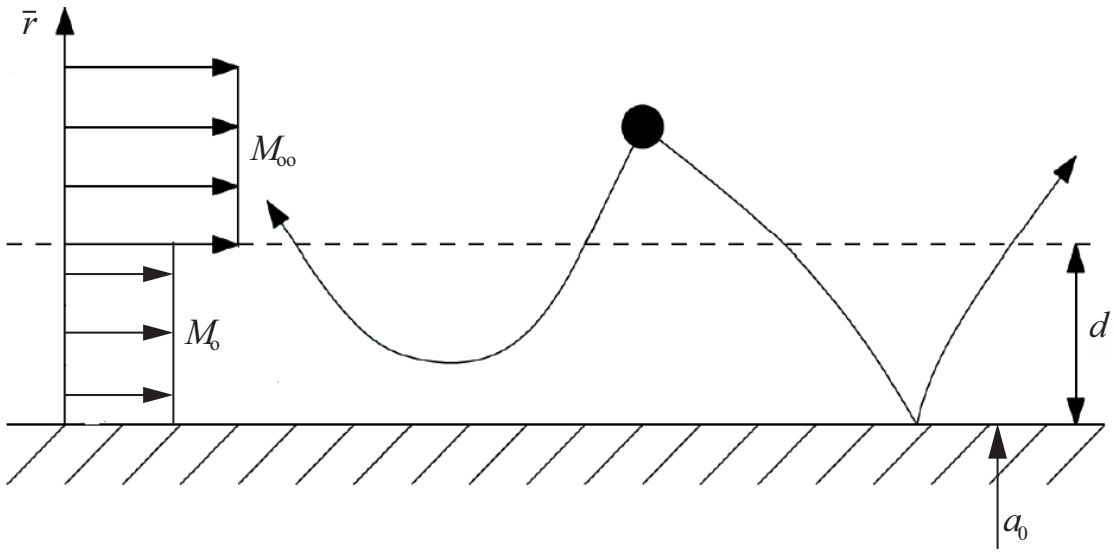

Fig. 3 Boundary layer with step-function velocity profile.

The total field inside the boundary layer, $a_0 < \bar{r} < a_0 + d$, is the solution of the homogeneous convected wave equation expressed in cylindrical polar coordinates $(\bar{r},\bar{\phi},\bar{z})$ centred on the cylinder. Thus the Fourier-transformed

pressure has the following form,

$$\overline{p'_{t0_n}}\left(\bar{r},k_z,t\right) \;=\; \frac{1}{2\pi}\left(A_n\left(k_z,\omega_0\right)\mathrm{J}_n\left(\Gamma_0\bar{r}\right)+B_n\left(k_z,\omega_0\right)\mathrm{H}_n^{(2)}\left(\Gamma_0\bar{r}\right)\right)\mathrm{e}^{\mathrm{i}\omega_0 t}, \tag{15}$$

where $\Gamma_0^2=(k_0+k_zM_0)^2-k_z^2$.

Outside the boundary layer, the solution is the same as in the previous section III.A, namely the sum of the incident and scattered field $\overline{p'_{t\infty_n}}=\overline{p'_{i\infty_n}}+\overline{p'_{s\infty_n}}$, with the incident field

$$\overline{p'_{i\infty_n}}\left(\bar{r},k_z,t\right) \;=\; E_n\left(k_z,\omega_0\right)\mathrm{J}_n\left(\Gamma_\infty\bar{r}\right)\mathrm{e}^{\mathrm{i}\omega_0 t} \quad \text{for} \quad a_0+d<\bar{r}<b, \tag{16}$$

where $E_n\left(k_z,\omega_0\right) = \pi^2\xi_{lq}P_{lq}\left(-1\right)^{(l+n)}\mathrm{e}^{-\mathrm{i}(l-n)\beta}\left(k_0+k_zM_\infty\right)\Psi_{lq}\,\mathrm{H}_{l-n}^{(2)}\left(\Gamma_\infty b\right)$, $\Gamma_\infty^2=(k_0+k_zM_\infty)^2-k_z^2$ and Ψ_{lq} is given by eqs. (6,7) with Γ_0 replaced by Γ_∞ (as shown in [16]). Note the change in the subscript, where ∞ denotes the involvement of the free stream Mach number M_∞, whereas 0 denotes the involvement of the inner Mach number M_0. The scattered field outside the boundary layer is once again the solution of the homogeneous convected wave equation, and in order to satisfy the same outward propagating conditions as in the previous section III.A, only a Hankel function term is used,

$$\overline{p'_{s\infty_n}}\left(\bar{r},k_z,t\right) \;=\; \frac{1}{2\pi}\,C_n\left(k_z,\omega_0\right)\mathrm{H}_n^{(2)}\left(\Gamma_\infty\bar{r}\right)\mathrm{e}^{\mathrm{i}\omega_0 t}. \tag{17}$$

The solutions inside and outside the layer are matched at the edge of the layer. The following boundary conditions are applied:

(1) hard-wall boundary condition on the surface of the cylinder

$$\frac{\partial\overline{p'_{t0_n}}}{\partial\bar{r}}=0 \quad \text{at} \quad \bar{r}=a_0; \tag{18}$$

(2) continuity of pressure at the edge of the boundary layer

$$\overline{p'_{t0_n}}=\overline{p'_{i\infty_n}}+\overline{p'_{s\infty_n}} \quad \text{at} \quad \bar{r}=a_0+d; \tag{19}$$

(3) continuity of particle displacement at the edge of the boundary layer (Hanson [2], Mariano [21], Ko [22], Eversman [14])

$$\frac{\partial\overline{p'_{t0_n}}}{\partial\bar{r}}\,\frac{1}{\left(k_0+k_zM_0\right)^2}=\left(\frac{\partial\overline{p'_{i\infty_n}}}{\partial\bar{r}}+\frac{\partial\overline{p'_{s\infty_n}}}{\partial\bar{r}}\right)\frac{1}{\left(k_0+k_zM_\infty\right)^2} \quad \text{at} \quad \bar{r}=a_0+d. \tag{20}$$

Using these three conditions, expressions for the coefficients $A_n\left(k_z,\omega_0\right)$, $B_n\left(k_z,\omega_0\right)$ and $C_n\left(k_z,\omega_0\right)$ can be obtained. With $A_n\left(k_z,\omega_0\right)$ and $B_n\left(k_z,\omega_0\right)$ known, the Fourier transformed total field inside the boundary layer can be recovered from eq.(15). Finally, by setting $\bar{r}=a_0$ and performing an inverse Fourier z-transform as in the previous section III.A, the solution for the pressure on the cylinder surface in real space is obtained:

$$p'_t\left(a_0,\bar{\phi},\bar{z},t\right) \;=\; -\xi_{lq}P_{lq}\left(-1\right)^l\mathrm{e}^{-\mathrm{i}l\beta}\,\mathrm{e}^{\mathrm{i}\omega_0 t}\sum_{n=-\infty}^{\infty}\left(-1\right)^n\mathrm{e}^{\mathrm{i}n\beta}\,I_n(a_0,\bar{z})\,\mathrm{e}^{-\mathrm{i}n\bar{\phi}}\,, \tag{21}$$

where

$$I_n(a_0,\bar{z})=\int_{-\infty}^{\infty}\frac{\left(k_0+k_zM_\infty\right)\Psi_{lq}\,\mathrm{H}_{l-n}^{(2)}\left(\Gamma_\infty b\right)}{\pi^2\Gamma_0\,a_0(a_0+d)\left(k_0+k_zM_\infty\right)^2D_n\left(k_z,\omega_0\right)\mathrm{H}_n^{(2)}\left(\Gamma_\infty(a_0+d)\right)\mathrm{J}'_n\left(\Gamma_0 a_0\right)}\,\mathrm{e}^{-\mathrm{i}k_z\bar{z}}\,\mathrm{d}k_z, \tag{22}$$

and

$$\begin{aligned}D_n\left(k_z,\omega_0\right)=&\left[\mathrm{H}_n^{(2)\prime}\left(\Gamma_0(a_0+d)\right)-\mathrm{J}'_n\left(\Gamma_0(a_0+d)\right)\frac{\mathrm{H}_n^{(2)\prime}\left(\Gamma_0 a_0\right)}{\mathrm{J}'_n\left(\Gamma_0 a_0\right)}\right]\frac{\Gamma_0}{\left(k_0+k_zM_0\right)^2}\\&-\left[\mathrm{H}_n^{(2)}\left(\Gamma_0(a_0+d)\right)-\mathrm{J}_n\left(\Gamma_0(a_0+d)\right)\frac{\mathrm{H}_n^{(2)\prime}\left(\Gamma_0 a_0\right)}{\mathrm{J}'_n\left(\Gamma_0 a_0\right)}\right]\frac{\Gamma_\infty}{\left(k_0+k_zM_\infty\right)^2}\,\frac{\mathrm{H}_n^{(2)\prime}\left(\Gamma_\infty(a_0+d)\right)}{\mathrm{H}_n^{(2)}\left(\Gamma_\infty(a_0+d)\right)}.\end{aligned} \tag{23}$$

Furthermore, with $C_n\,(k_z, \omega_0)$ known, the Fourier transformed scattered field outside the boundary layer is recovered from eq. (17). The outside scattered field is essential in order to obtain the total far-field.

Performing a similar procedure using the far-field expression for the incident field given by eq. (8) with Γ_∞ instead of Γ_0, the final far-field expression is obtained:

$$\begin{aligned} p'_{t_{ff}}\,(\bar{R},\bar{\phi},\bar{\theta},t) =& \frac{\mathrm{i}\xi_{lq}P_{lq}\,k_0\,\Psi_{lq}(\Delta_\infty)}{2\bar{R}}\,\frac{S\,(\bar{\theta})}{(1-M_\infty^2\sin^2\bar{\theta})}\,\mathrm{e}^{\mathrm{i}\omega_0 t}\,\mathrm{e}^{-\mathrm{i}k_0\bar{R}S(\bar{\theta})}\sum_{n=-\infty}^{\infty}\mathrm{e}^{\mathrm{i}(n-l)\beta}\,\mathrm{e}^{\frac{1}{2}n\pi\mathrm{i}}\times \\ & \left[\mathrm{J}_{n-l}\,(\Delta_\infty b)+\left[\frac{2\mathrm{i}\,(1-M_\infty^2\sin^2\bar{\theta})\,\Upsilon_n\,(\Delta_0)}{\pi(a_0+d)\,\mathrm{H}_n^{(2)}\,(\Delta_\infty(a_0+d))\,k_0^2\,S^2\,(\bar{\theta})\,D_n\,(\Delta_\infty,\Delta_0)}\right.\right. \\ & \left.\left.-\,\mathrm{J}_n\,(\Delta_\infty(a_0+d))\right]\frac{\mathrm{H}_{n-l}^{(2)}\,(\Delta_\infty b)}{\mathrm{H}_n^{(2)}\,(\Delta_\infty(a_0+d))}\right]\mathrm{e}^{-\mathrm{i}n\bar{\phi}}\,, \end{aligned} \tag{24}$$

where

$$\begin{aligned} D_n\,(\Delta_\infty,\Delta_0) =& \left[\mathrm{H}_n^{(2)\prime}\,(\Delta_0(a_0+d))-\mathrm{J}'_n\,(\Delta_0(a_0+d))\,\frac{\mathrm{H}_n^{(2)\prime}\,(\Delta_0 a_0)}{\mathrm{J}'_n\,(\Delta_0 a_0)}\right] \\ & \times\frac{\Delta_0}{k_0^2\big(1+\frac{C\,(\bar{\theta})\,M_0}{(1-M_\infty^2\sin^2\bar{\theta})^{1/2}}\big)^2} \\ & -\left[\mathrm{H}_n^{(2)}\,(\Delta_0(a_0+d))-\mathrm{J}_n\,(\Delta_0(a_0+d))\,\frac{\mathrm{H}_n^{(2)\prime}\,(\Delta_0 a_0)}{\mathrm{J}'_n\,(\Delta_0 a_0)}\right] \\ & \times\frac{\sin\bar{\theta}(1-M_\infty^2\sin^2\bar{\theta})^{1/2}}{k_0\,S^2\,(\bar{\theta})}\,\frac{\mathrm{H}_n^{(2)\prime}\,(\Delta_\infty(a_0+d))}{\mathrm{H}_n^{(2)}\,(\Delta_\infty(a_0+d))}, \end{aligned} \tag{25}$$

and $\Delta_\infty=\frac{k_0\sin\bar{\theta}}{(1-M_\infty^2\sin^2\bar{\theta})^{1/2}}$, $\Upsilon_n\,(\Delta_0)=\left[\mathrm{H}_n^{(2)}\,(\Delta_0(a_0{+}d))-\mathrm{J}_n\,(\Delta_0(a_0{+}d))\,\frac{\mathrm{H}_n^{(2)\prime}(\Delta_0 a_0)}{\mathrm{J}'_n\,(\Delta_0 a_0)}\right]$, $C(\bar{\theta})=\frac{\left(\cos\bar{\theta}+M_\infty(1-M_\infty^2\sin^2\bar{\theta})^{1/2}\right)}{\sigma_\infty^2}$, and finally

$$\Delta_0=\frac{k_0}{(1-M_\infty^2\sin^2\bar{\theta})^{1/2}}\sqrt{(1-M_\infty^2\sin^2\bar{\theta})+C\,(\bar{\theta})[2M_0(1-M_\infty^2\sin^2\bar{\theta})^{1/2}-C\,(\bar{\theta})\sigma_0^2]}. \tag{26}$$

The procedure and details of the derivation of eq. (24) is very similar to that used in section III.A, and is given in full in the appendix of Rouvas & McAlpine [6]. Equations (21) and (24) are validated by reducing the boundary layer to a uniform flow. Indeed, when $M_0 \to M_\infty$, eqs. (21) and (24) converge to eqs. (12) and (14) respectively which are the uniform flow solutions.

C. Linear Boundary-Layer Profile Analysis

As stated in section II, there are two ways identified to solve analytically the Pridmore-Brown equation by assuming a linear shear velocity profile. Either the method proposed by Goldstein and Rice [15] or the asymptotic method by Eversman and Beckemeyer[14]. The work presented here in brief summary is given in full detail in the paper by Rouvas and McAlpine [6] which uses the asymptotic method proposed by Eversman and Beckemeyer [14].

The analysis begins with the Fourier-transformed Pridmore-Brown equation which describes the total field inside a linear boundary-layer with slip on the wall M_w and free stream Mach number M_∞.

$$\frac{\mathrm{d}^2\overline{p'_{t_{in}}}}{\mathrm{d}\bar{r}^2}+\left(\frac{1}{\bar{r}}-\frac{2k_zM'}{k_0+k_zM}\right)\frac{\mathrm{d}\overline{p'_{t_{in}}}}{\mathrm{d}\bar{r}}+\left[(k_0+k_zM)^2-k_z^2-\frac{n^2}{\bar{r}^2}\right]\overline{p'_{t_{in}}}=0. \tag{27}$$

By introducing the variable $y=\frac{\bar{r}-a_0}{a_0}$ and the parameters $\varepsilon=\frac{d}{a_0}$, $\zeta=\frac{y}{\varepsilon}$, and with the distribution of Mach number inside the boundary layer $M(y)=M_\infty\varphi(\zeta)=M_\infty(\zeta\frac{M_\infty-M_w}{M_\infty}+\frac{M_w}{M_\infty})$, eq.(27) can be rewritten as

$$\frac{\mathrm{d}^2\overline{p'_{t_{in}}}}{\mathrm{d}\zeta^2}+\left(\frac{\varepsilon}{\varepsilon\zeta+1}-\frac{2KM_\infty}{1+KM}\frac{\mathrm{d}\varphi}{\mathrm{d}\zeta}\right)\frac{\mathrm{d}\overline{p'_{t_{in}}}}{\mathrm{d}\zeta}+\varepsilon^2\left[(k_0a_0)^2\left[(1+KM)^2-K^2\right]-\frac{n^2}{(\varepsilon\zeta+1)^2}\right]\overline{p'_{t_{in}}}=0, \tag{28}$$

where $K = k_z/k_0$. This equation can be solved for small values of the parameter ε using a power series solution,

$$\overline{p'_{t_{in}}}(\zeta) = \overline{p_0}(\zeta) + \varepsilon\overline{p_1}(\zeta) + \varepsilon^2\overline{p_2}(\zeta) + \varepsilon^3\overline{p_3}(\zeta) + \dots \tag{29}$$

By substituting this solution into eq. (28), the pressure inside the boundary layer can be obtained in terms of integral equations which are solvable for a linear boundary-layer profile.

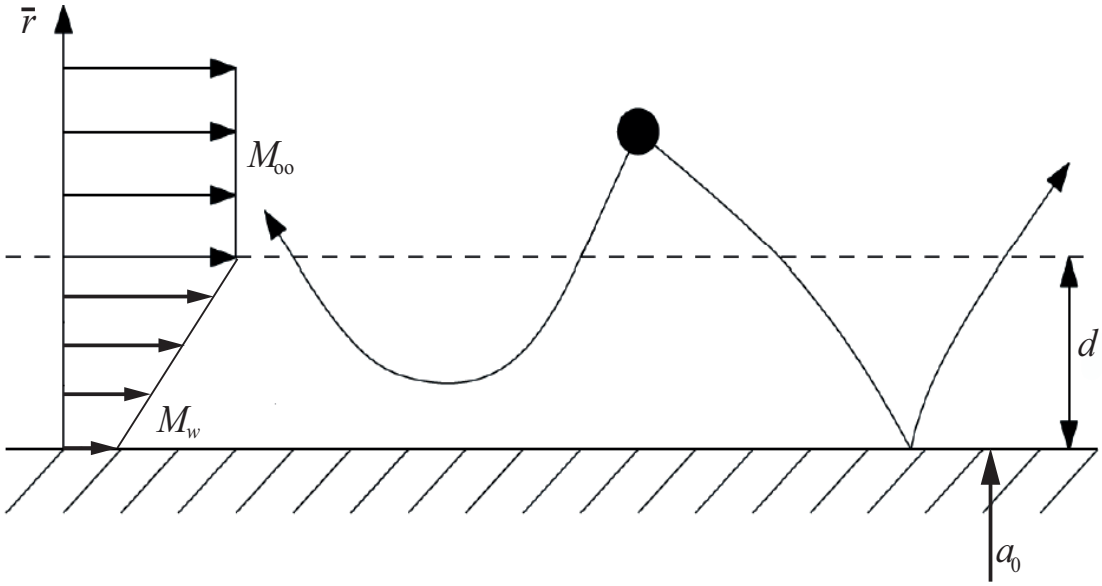

Fig. 4 Boundary layer with linear velocity profile.

The solution outside the layer is described as before with eqs. (16) and (17). These are matched with the solution inside the layer using the same boundary conditions at the edge of the boundary layer as before, namely continuity of pressure (eq.(19)) and continuity of particle displacement (eq.(20)), which in this case reduces to continuity of pressure gradient. Finally, by setting $\bar{r} = a_0$, and then performing an inverse Fourier z-transform, the expression for the pressure on the surface of the cylindrical fuselage is obtained:

$$p'_{t_{in}}(a_0, \bar{\phi}, \bar{z}, t) = \frac{\xi_{lq} P_{lq}}{4} (-1)^l \, \mathrm{e}^{-\mathrm{i}l\beta} \, \mathrm{e}^{\mathrm{i}\omega_0 t} \sum_{n=-\infty}^{\infty} \left\{ (-1)^n \, \mathrm{e}^{\mathrm{i}n\beta} \, I_n(a_0, \bar{z}) \, \mathrm{e}^{-\mathrm{i}n\bar{\phi}} \right\}, \tag{30}$$

where

$$I_n(a_0, \bar{z}) = \int_{-\infty}^{\infty} (k_0 + k_z M_\infty) \, \Psi_{lq} \, \mathrm{H}^{(2)}_{l-n}(\Gamma_\infty b) \, S_n(k_z, \omega_0) \mathrm{e}^{-\mathrm{i}k_z \bar{z}} \, \mathrm{d}k_z, \tag{31}$$

and

$$\begin{aligned} S_n(k_z, \omega_0) = & \frac{\mathrm{J}_n(\Gamma_\infty(a_0+d))}{G} \\ & + \frac{\left[\mathrm{J}'_n(\Gamma_\infty(a_0+d)) - \frac{R}{G} \frac{\varepsilon}{\Gamma_\infty a_0} (1 + KM_\infty)^2 \mathrm{J}_n(\Gamma_\infty(a_0+d)) \right]}{\left[\frac{R}{G} \frac{\varepsilon}{\Gamma_\infty a_0} (1 + KM_\infty)^2 \mathrm{H}^{(2)}_n(\Gamma_\infty(a_0+d)) - \mathrm{H}^{(2)\prime}_n(\Gamma_\infty(a_0+d)) \right]} \frac{\mathrm{H}^{(2)}_n(\Gamma_\infty(a_0+d))}{G}, \end{aligned} \tag{32}$$

$$R = \mu\left(\frac{1}{g} - \frac{1}{s^2+g}\right) - \nu - \varepsilon\left[\frac{2n^2-\mu}{s^2} \ln(s^2/g+1) - \frac{2n^2}{s^2+g} + \frac{\mu}{g} - \frac{\nu}{2}\right], \tag{33}$$

$$G = 1 + \varepsilon^2\left[\mu\left(\frac{s^2}{3g} + 1/2\right) - \nu\left(\frac{s^2}{4} + 2g/3 + \frac{g^2}{2s^2}\right)\right], \tag{34}$$

and $\nu = (k_0 a_0)^2$, $\mu = \nu K^2 + n^2$, $s = K(M_\infty - M_w)$ and $g = s(1 + KM_w)$.

Equations (30) and (31) have been initially validated. In the limit as the effective boundary-layer thickness reduces to zero, $d \to 0$, equations (30) and (31) reduce to the uniform flow case, namely eqs. (12) and (13) respectively.

Finally, the far-field expression is presented whose full derivation can be found in Ref. [6] The final total far-field in real space is

$$p'_{t_{ff}}(\bar{R},\bar{\theta},\bar{\phi},t) = \frac{\mathrm{i}\xi_{lq}P_{lq}k_0}{2\bar{R}}\frac{S(\bar{\theta})}{\Theta}\Psi_{lq}(\Delta_\infty)\,\mathrm{e}^{\mathrm{i}\omega_0 t}\,\mathrm{e}^{-\mathrm{i}k_0\bar{R}S(\bar{\theta})}\sum_{n=-\infty}^{\infty}\mathfrak{C}_n(\bar{\theta})\mathrm{e}^{-\mathrm{i}(l-n)\beta}\mathrm{e}^{\frac{1}{2}n\pi\mathrm{i}}\mathrm{e}^{-\mathrm{i}n\bar{\phi}}, \tag{35}$$

where

$$\mathfrak{C}_n(\bar{\theta}) = \left[\mathrm{J}_{n-l}(\Delta_\infty b) + \mathrm{H}^{(2)}_{n-l}(\Delta_\infty b)\frac{\left[\mathrm{J}'_n(\Delta_\infty(a_0+d)) - \frac{R(\bar{\theta})}{G(\bar{\theta})}\frac{\varepsilon(\Theta^{1/2}+M_\infty C(\bar{\theta}))^2}{k_0 a_0\sin\bar{\theta}\Theta^{1/2}}\mathrm{J}_n(\Delta_\infty(a_0+d))\right]}{\left[\frac{R(\bar{\theta})}{G(\bar{\theta})}\frac{\varepsilon(\Theta^{1/2}+M_\infty C(\bar{\theta}))^2}{k_0 a_0\sin\bar{\theta}\Theta^{1/2}}\mathrm{H}^{(2)}_n(\Delta_\infty(a_0+d)) - \mathrm{H}^{(2)\prime}_n(\Delta_\infty(a_0+d))\right]}\right], \tag{36}$$

with

$$\begin{aligned} G(\bar{\theta}) = &\left\{1+\varepsilon^2\left[\left(n^2+\nu\frac{C^2(\bar{\theta})}{\Theta}\right)\left[\frac{C(\bar{\theta})(2M_\infty+M_w)+3\Theta^{1/2}}{6\left(\Theta^{1/2}+M_wC(\bar{\theta})\right)}\right]\right.\right. \\ &\left.\left. -\frac{\nu}{\Theta}\left[\frac{C^2(\bar{\theta})(M_\infty-M_w)^2}{4}+\left(\Theta^{1/2}+M_wC(\bar{\theta})\right)\left(C(\bar{\theta})(\frac{2}{3}M_\infty-\frac{1}{6}M_w)+\frac{1}{2}\Theta^{1/2}\right)\right]\right]\right\}, \end{aligned} \tag{37}$$

and

$$\begin{aligned} R(\bar{\theta}) = &\left\{\frac{\nu C^2(\bar{\theta})+n^2\Theta}{\left(\Theta^{1/2}+M_wC(\bar{\theta})\right)\left(\Theta^{1/2}+M_\infty C(\bar{\theta})\right)}-\nu\right. \\ &-\varepsilon\left[\frac{n^2\Theta}{C^2(\bar{\theta})(M_\infty-M_w)}\left[C(\bar{\theta})\left(\frac{C(\bar{\theta})(M_\infty-2M_w)-\Theta^{1/2}}{\left(\Theta^{1/2}+M_wC(\bar{\theta})\right)\left(\Theta^{1/2}+M_\infty C(\bar{\theta})\right)}\right)+\frac{1}{(M_\infty-M_w)}\ln\left(\frac{\Theta^{1/2}+M_\infty C(\bar{\theta})}{\Theta^{1/2}+M_wC(\bar{\theta})}\right)\right]\right. \\ &\left.\left.+\frac{\nu}{(M_\infty-M_w)}\left[\frac{C(\bar{\theta})}{\left(\Theta^{1/2}+M_wC(\bar{\theta})\right)}-\frac{(M_\infty-M_w)}{2}-\frac{1}{(M_\infty-M_w)}\ln\left(\frac{\Theta^{1/2}+M_\infty C(\bar{\theta})}{\Theta^{1/2}+M_wC(\bar{\theta})}\right)\right]\right]\right\}. \end{aligned} \tag{38}$$

Also, $\Delta_\infty = \frac{k_0\sin\bar{\theta}}{(1-M\infty^2\sin^2\bar{\theta})^{1/2}}$, $\Theta = (1-M_\infty^2\sin^2\bar{\theta})$, $S(\bar{\theta}) = \frac{\left(\Theta^{1/2}+M_\infty\cos\bar{\theta}\right)}{\sigma_\infty^2}$, $C(\bar{\theta}) = \frac{\left(\cos\bar{\theta}+M_\infty\Theta^{1/2}\right)}{\sigma_\infty^2}$ and $\sigma_\infty^2 = 1-M_\infty^2$.

Note that eq. (35) is the same as its uniform flow equivalent in eq. (14) apart from the bracketed term $\mathfrak{C}_n(\bar{\theta})$. As before eq. (35) is validated by taking the limit as $d \to 0$. The bracketed term reduces to

$$\mathfrak{C}_n(\bar{\theta}) = \left[\mathrm{J}_{n-l}(\Delta_\infty b) + \mathrm{H}^{(2)}_{n-l}(\Delta_\infty b)\frac{\mathrm{J}'_n(\Delta_\infty a_0)}{-\mathrm{H}^{(2)\prime}_n(\Delta_\infty a_0)}\right], \tag{39}$$

which is the same as the bracketed term in eq. (14), showing that the linear-profile expression reduces to the uniform-flow expression.

IV. Validation

This section includes validation results that demonstrate the validity of the key equations in sections III.B and III.C. Moreover, the best method of replacing the actual velocity profile with a simplified model profile is investigated. The aim is to show that the step-function profile can be used to successfully quantify the refraction effect of a realistic turbulent boundary-layer profile, modelled by a 1/7th power-law profile. In all of the following examples, the geometric parameters and flight conditions are fixed and representative of typical values. The free-stream Mach number is 0.75 which is typical for cruise flight at 30.000 ft. The non-dimensional frequency represented by a Helmholtz number is chosen as $k_0a = 20$, a value that is relatively high for cruising conditions but quite representative for an aircraft during climb. All other aircraft dimensions are normalised with the fuselage radius which is taken to be unity, $a_0 = 1$. The

dimensions represent a typical wide-body aircraft configuration. The mode of propagation will be fixed at $(l, q) = (4, 1)$ which is a well cut-on mode. The results are presented either by SPL pressure contours on the surface of the fuselage, or in the form of the difference between the SPL with the boundary layer (calculated with eqs. (21) or (30)) and without the boundary layer (calculated with eq.(12)), defined by $\Delta_{bl} = \text{SPL}_{bl} - \text{SPL}$. Finally, in all of the examples the plane of the source is located at $\bar{z} = 0$ and at $\bar{\phi} = 0^{\text{o}}$.

Rouvas & McAlpine [10] investigated an approach for creating an equivalent linear velocity profile that best simulates the refraction effects of a 1/7th power-law profile. Three different methods were investigated. Equating the shape factor of the two profiles, equating boundary-layer and displacement thickness of the two profiles, or equating boundary-layer and momentum thickness of the two profiles. When each of these methods are applied, appropriate values are obtained for the equivalent linear boundary-layer thickness (effective thickness d) and Mach at the wall M_w. The same applies for the equivalent step-function boundary-layer, where appropriate values for the effective thickness d and internal Mach number M_0 are obtained. Figure (5) illustrates how these equivalent profiles and their effective thicknesses compare with the original 1/7th power-law profile with thickness δ. As expected the effective thickness d is smaller than δ for the shape factor method [2].

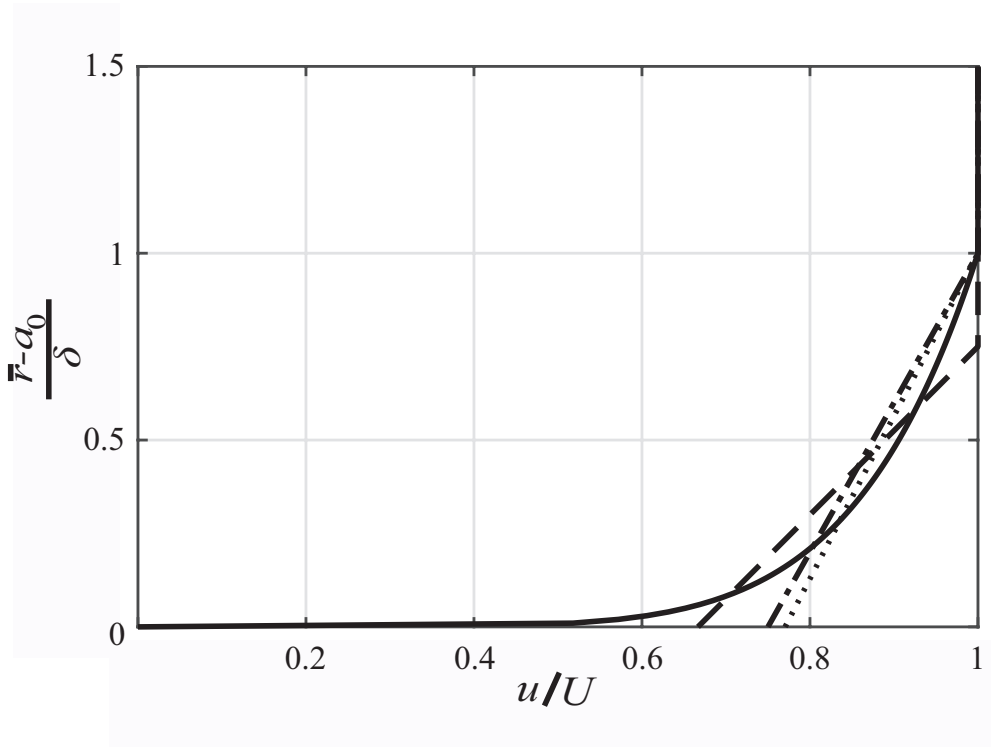

Fig. 5 The three equivalent linear velocity profiles, equal shape factor (dashed line), equal boundary-layer and displacement thickness (dash-dotted line), equal boundary-layer and momentum thickness (dotted line) are plotted compared to the actual 1/7th power law profile (solid line).

By examining the Δ_{bl} in Fig. (6), the importance of the refraction effect caused by the presence of the boundary-layer upstream of the source is clearly seen. Sound propagating upstream refracts away from the surface and shielding takes place over the entire upstream area. It is also apparent that the optimal method for matching the turbulent power-law profile is the equal shape factor. Both the equivalent linear and step-function profiles with equal shape factor to the original power-law profile give predictions that are remarkably close to the numerical results, for this boundary-layer thickness. Both these equivalent profiles prove to be able to approximate the amplitude and modal pattern of the shielding effect. All remaining examples will use the equal shape factor as a matching method to approximate the power-law profile.

Figures (7) and (8) show the Sound Pressure Level (SPL) on the surface of the fuselage. In both figures the shadow zone is located at the "back" of the cylinder ($\bar{\phi} = 180^{\text{o}}$) as expected, since the source is located at the near side of the cylinder ($\bar{\phi} = 0^{\text{o}}$), thus the far side of the cylinder is not in a direct line of sight of the source. In both figures the

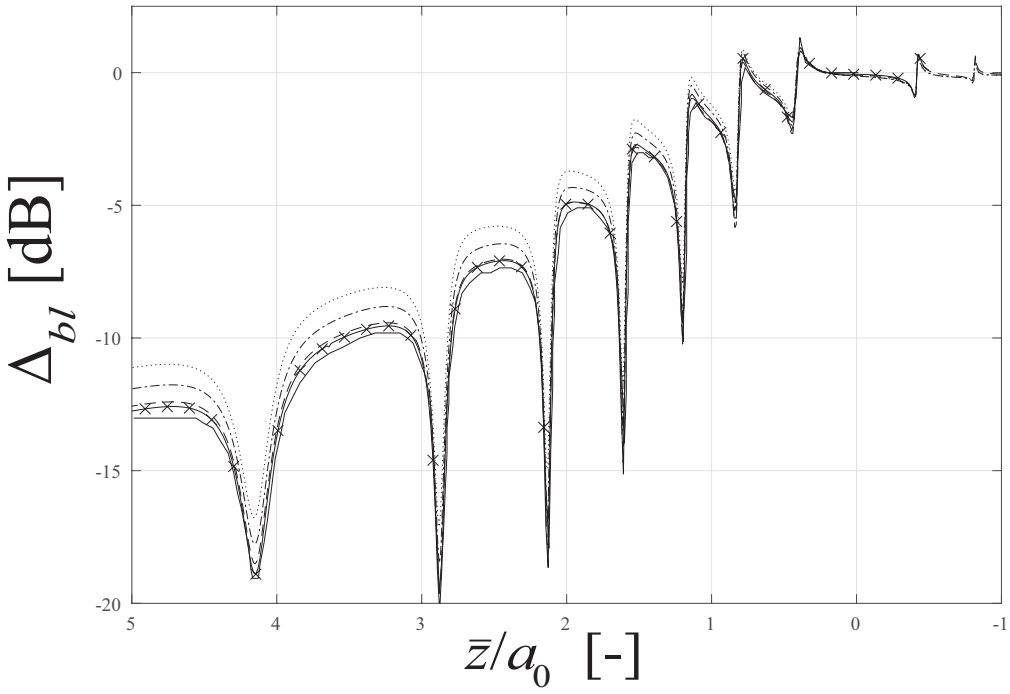

Fig. 6 Δ_{bl} **at** $\bar{\phi} = 0$ **for the step-function and linear velocity profiles compared with numerical predictions taken from [17]. Key: Numerical result for a 1/7th power-law profile (solid line); Linear velocity profiles (recreated from Ref. [10]) with equal shape factor (dashed line), equal boundary-layer and displacement thickness (dash-dotted line), or equal boundary-layer and momentum thickness (dotted line); Step-function profile with equal shape factor (solid line(×)). The other parameters are:** $(l, q) = (4, 1)$**,** $a = 0.5a_0$**,** $b = 3a_0$**,** $M_\infty = 0.75$**,** $k_0 a = 20$ **and** $\delta = 0.01a_0$**.**

discrepancies are barely visible on the near side of the cylinder. Both the equivalent profiles successfully simulate the predicted pressure levels calculated by the numerical method with a 1/7th power-law profile. The only discrepancies visible are located in the shadow zone. However, the shadow zone generally exhibits pressure levels at least 100 dB lower than the near side of the cylinder effectively reaching the numerical noise floor. Therefore, these minuscule differences in the shadow zone are irrelevant.

The results presented thus far are for a relatively thin boundary layer of 1% of the fuselage radius. The accuracy of the results is expected to deteriorate for thicker layers as is evident from the mathematical formulation of the linear velocity profile, which assumes that the boundary-layer thickness is sufficiently small compared to the fuselage radius, (see parameter ε in section III.C and in [6], [10]). This is demonstrated in Fig. (9) where the equivalent linear profile struggles to approximate the shielding effect of the power-law profile for larger boundary-layer thicknesses. On the other hand, the equivalent step-function profile exhibits remarkably similar behaviour at thicker boundary layers. This is because the step-function boundary-layer analysis does not involve the boundary-layer thickness limitation mentioned in the linear profile analysis, and so the equivalent step-function profile approximation retains the same accuracy regardless of the thickness. A case could be made here that the equivalent linear profile could be used to approximate thinner boundary layers, while an equivalent step-function profile should be used for thicker boundary layers.

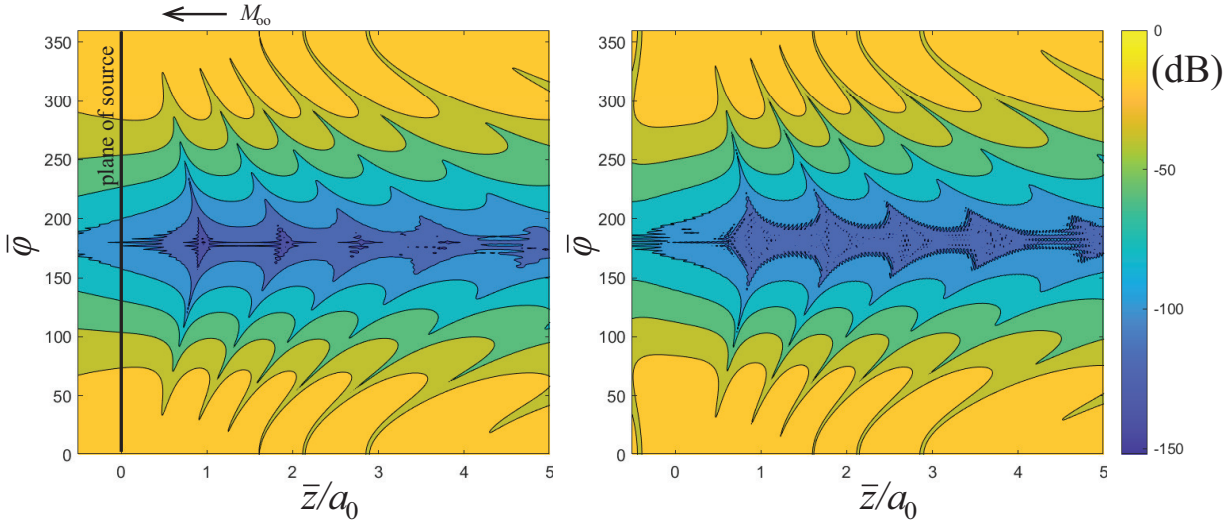

Fig. 7 SPL on the surface of the fuselage, normalised so that the maximum SPL is at 0 dB. Comparison of numerical results [left] for a 1/7th power-law boundary layer calculated with the code developed by Gaffney [17], and theoretical results [right] generated using an equivalent linear profile. The other parameters are: $(l, q) = (4, 1)$**,** $a = 0.5a_0$**,** $b = 3a_0$**,** $M_{\infty} = 0.75$**,** $k_0 a = 20$**,** $\delta = 0.01a_0$ **and 1/7th power law profile.**

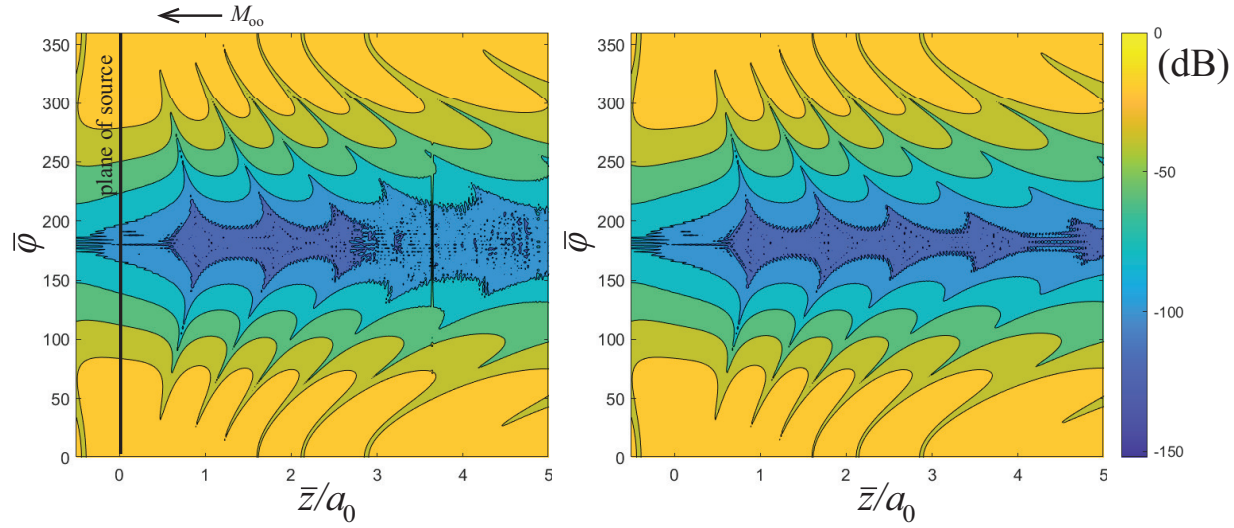

Fig. 8 SPL on the surface of the fuselage, normalised so that the maximum SPL is at 0 dB. Comparison of theoretical results [left] generated using an equivalent step-function profile, and theoretical results [right] generated using an equivalent linear profile, based on matching the simplified model profiles to a 1/7th power-law boundary layer. The other parameters are: $(l, q) = (4, 1)$**,** $a = 0.5a_0$**,** $b = 3a_0$**,** $M_{\infty} = 0.75$**,** $k_0 a = 20$**,** $\delta = 0.01a_0$**.**

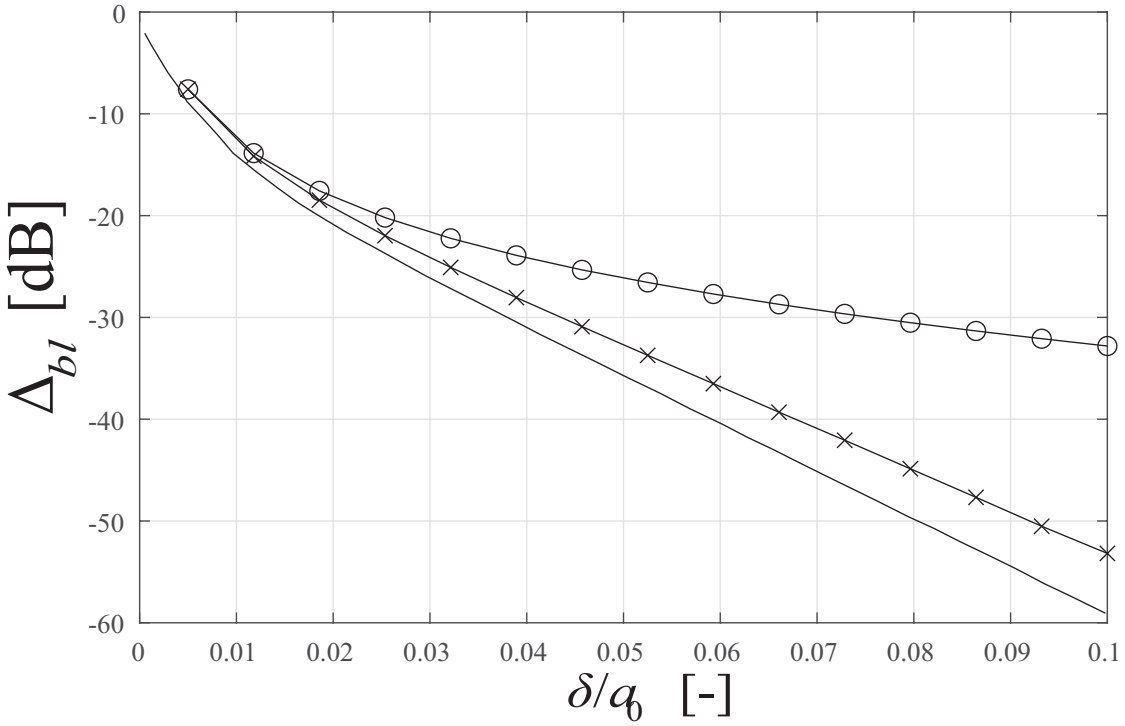

Fig. 9 Δ_{bl} **at** $\bar{\phi} = 0$ **and** $\bar{z} = 5a_0$ **versus the non-dimensional 1/7th power-law boundary-layer thickness. Comparison of theoretical results generated using an equivalent linear profile (◯), or an equivalent step-function profile (×), and numerical results for the actual 1/7th power-law boundary layer (no marker). The other parameters are:** $(l, q) = (4, 1)$**,** $a = 0.5a_0$**,** $b = 3a_0$**,** $M_\infty = 0.75$**,** $k_0 a = 20$**.**

V. Results

Having established that both the linear and the step-function velocity profiles can approximate the effect of a realistic turbulent boundary-layer, modelled by a 1/7th power-law profile, further investigation into the shielding effect has been carried out in the form of a parametric study. This study involves realistic dimensions, configurations, flight parameters and conditions. The SPL on the fuselage surface is calculated using eqs. (21) and (30), and directivity plots are calculated using the far-field expressions in eqs. (24) and (35).

A. Construction of the Model

In recent years turbofan engines have tended to become larger with higher by-pass ratios. The dimensions for a typical wide-body aircraft are chosen since that type of aircraft is more likely to be equipped with an ultra high by-pass ratio engine. The dimensions of the representative model are shown in table (1). All the length parameters are normalised by the fuselage radius, a_0.

Parameter	Value
a/a_0	0.5
b/a_0	3.5
β	0^o
$\bar{z}_{ps}/a_0$	0
$\bar{z}_{ec}/a_0$	4
$\bar{\theta}_{ff}$	[5^o,175^o]
$\bar{\phi}_{ff}$	$3\frac{\pi}{2}$

Table 1 Dimensions of parametric study model.

The parameters $\bar{z}_{ps}$ and $\bar{z}_{ec}$, respectively the position of the plane of the source (the plane of the fan inlet), and the position of the end of the nose cone, also represent the axial range of the calculations for the fuselage surface pressure results. This range of $\bar{z}$ represents the entire section of the fuselage upstream of the source that can be approximated by a cylinder with constant radius. Beyond $\bar{z}_{ec}$, the nose cone structure cannot be modelled by the current theoretical formulation. The parameters $\bar{\theta}_{ff}$ and $\bar{\phi}_{ff}$ refer to the grid for the far-field calculations. The expressions in eqs. (24) and (35) can give the far-field pressure at any point $(\bar{\theta}, \bar{\phi})$ on a sphere of radius $\bar{R}$ centered on the fuselage. In this study, results for a hemisphere directly beneath the flight path, $\bar{\phi} = 3\frac{\pi}{2}$, are produced since this directivity pattern propagates towards the ground. Note that extreme values of polar angles $\bar{\theta}$, close to 0° or 180°, are excluded to avoid any numerical singularities.

The range of the $\bar{z}$-grid points, from $\bar{z}_{ps}$ to $\bar{z}_{ec}$, dictate the values used for the boundary-layer thickness δ. Flat plate theory is assumed for the growth of the boundary layer. This means that the relationship $\delta(x) = 0.37x/\mathrm{Re}_x^{1/5}$ is used, where x is the distance taken from the nose of the fuselage. In the parametric study, three different constant boundary-layer thicknesses are considered: thin, thick and average. The thin boundary layer has a constant thickness equal to that of the boundary layer at the end of the nose cone, whilst the thick boundary layer has a constant thickness equal to that of the boundary layer at the plane of the source. The constant thickness of the average boundary layer is calculated by integrating the boundary-layer thickness over the axial range, which gives a more realistic average than a simple arithmetic mean of the thin and thick layers.

The operating conditions of the study are determined by the cut-off ratio of the dominant rotor-locked mode. Assuming that there are no instabilities in the fan inlet flow, the rotor-locked mode has azimuthal order equal to the number of blades of the fan. In the case presented here the number of blades is taken to be $B = 20$, which is a typical value for a high by-pass ratio engine used on a wide-body aircraft. Therefore the dominant mode is $(l, q) = (20, 1)$. For the example presented in this paper, the cut-off ratio of the rotor-locked mode is chosen to be $\zeta = 1.4$, which is reasonably well cut-on. This means that the non-dimensional blade passing frequency (BPF) is equal to $k_0 a = 23.6$, which corresponds to approximately 90 % of the engine nominal maximum rpm, (and is a realistic value for an ultra high by-pass ratio engine). The climbing stage is typically characterised by relatively high engine rpm/high BPF, which gradually reduce as the aircraft approaches cruising altitude and conditions. Thus, the remainder of the operating conditions and parameters are chosen to represent a typical climbing stage of the flight. The chosen flight Mach

number $M_\infty = 0.65$, and the altitude is set at 7000m. For this flight Mach number and altitude the three boundary-layer thicknesses are calculated to be: thin $0.032a_0$, average $0.047a_0$, and thick $0.061a_0$.

The simulation results in this paper include the contribution of every mode that is cut-on at the specified operating condition. To obtain the total contribution of all the modes, their pressures are summed incoherently. However, before summing the mean square pressures, the modal pressure amplitudes are adjusted (from their default value of unity) to specify the modal sound power distribution of the cut-on modes. The absolute square of the modal pressure amplitude is given in [16] by

$$|P_{lq}|^2 = \frac{2\rho_0 c_0 W_{lq}}{\pi\left[a^2 - \left(\frac{l}{\kappa_{lq}}\right)^2\right] \mathrm{J}_l^2(\kappa_{lq}a)[(1+M_\infty^2)\,\mathrm{Re}(\xi_{lq}) - M_\infty(1+|\xi_{lq}|^2)]}, \tag{40}$$

where W_{lq} is the modal sound power. An appropriate value for W_{lq} must be selected for each mode. In this parametric study, three types of source distribution are used based on previous findings ([23], [24]). (1) The equal energy source denoted by W_t^{ee}, where the total sound power of unity, $W_t = 1$, is divided equally among the modes, thus each mode has the same modal sound power $W_{lq} = W_t/\text{number of modes}$. (2) The rotor-locked source denoted by W_t^{20}, where the total sound power of unity, $W_t = 1$, is divided equally among the modes except for the rotor-locked mode (20,1) which has 100 times larger modal sound power (or 20 dB higher in PWL terms). (3) The rotor-locked source denoted by W_t^{30}, where the total sound power of unity, $W_t = 1$, is divided equally among the modes except from the rotor-locked mode (20,1) which has 1000 times larger modal sound power (or 30 dB higher in PWL terms).

According to previous research ([23], [24]) the most realistic of these prescribed sources is likely to be the W_t^{20} source, since in previously reported experimental measurements the dominant rotor-locked mode can exhibit an amplitude around 20 dB higher than the rest of the cut-on modes. Nonetheless, the equal energy source, W_t^{ee}, is very useful in order to create a baseline. It is also not uncommon for the rotor-locked mode to exhibit a level up to 30 dB higher, thus the source W_t^{30} should give further insight into the distribution and propagation of sound power.

B. Power Distribution and Thickness Effect

The difference between the sound power distributions of the three sources is demonstrated in Figs. (10) and (11). For the results in this section, the power-law boundary-layer profile is approximated using a linear equivalent profile via eq. (30). The differences in the results between the linear and the step-function velocity profiles are investigated in the next section of this paper. The cylinder plots in Fig. (10) showing the sound pressure levels on the fuselage surface highlight the importance of the presence of a dominant rotor-locked mode. Source W_t^{ee} exhibits a largely smooth contour pattern, which is consistent with multi-modal analysis, and an area of high SPL slightly upstream of the source plane. This is expected because the modes with higher cut-off ratios have principal lobes with smaller propagation angles. Owing to this, these modes are incident on the boundary layer further upstream, at shallow angles, making them more susceptible to refraction and less efficient at transmitting sound energy to the fuselage's surface. Modes with lower cut-off ratios have principal lobes with larger propagation angles. Owing to this, these modes are incident on the boundary layer near the source plane, at steeper angles, making them less susceptible to refraction and more easily able to transmit sound energy to the fuselage's surface.

On the other hand, when there is a rotor-locked mode present, the area of the maximum SPL is more distinctive and localised. This is because that is the area where the dominant mode's principal lobe is incident on the fuselage, resulting in high levels at that specific area. For the most realistic source W_t^{20}, there is a small area downstream of the principal lobe that exhibits similar pressure levels to the area where the dominant lobe is incident on the fuselage. This is because further downstream the shielding becomes less and less effective as explained before. This is the contribution from modes with lower cut-off ratios compared to the rotor-locked mode that are incident on the fuselage near the source plane. However, for the source W_t^{30}, also the secondary lobe is observed to contribute a distinctive area on the fuselage with high pressure levels localised in that area, as well as the dominant principal lobe.

Another metric that can be used to investigate the different results between the sources is the Δ_{source},

$$\Delta^i_{\text{source}} = \text{SPL}_i - \text{SPL}_{\text{ee}}, \tag{41}$$

where SPL_{ee} is the SPL calculated with the equal energy source W_t^{ee}, whilst i denotes either 20 or 30 representing values calculated for the sources W_t^{20} or W_t^{30} respectively. Using this metric and plotting it for $\bar{\phi} = 0$ as in Fig. (11), the difference between the equal energy source and the rotor-locked source is seen. The largest difference occurs upstream of the source position where the principal lobe of the rotor-locked mode is incident on the cylinder. It is apparent that

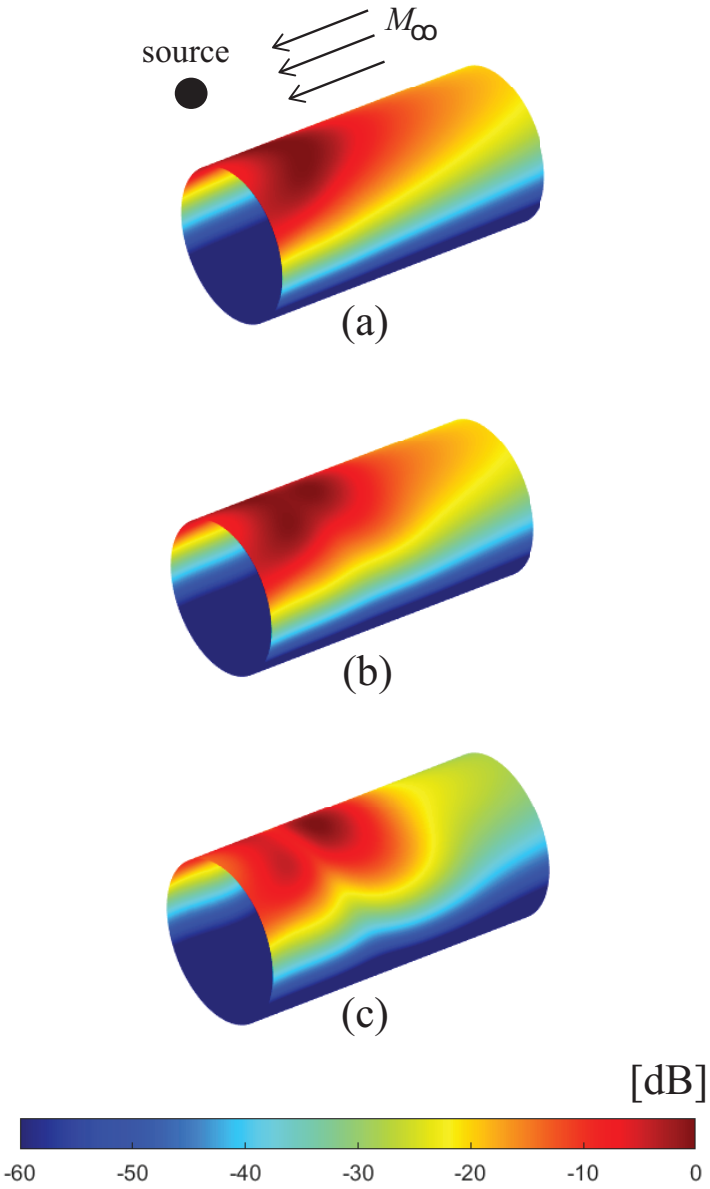

Fig. 10 SPL on the surface of the cylindrical fuselage for the three different sources and average boundary layer thickness. [(a)] W_t^{ee}, [(b)] W_t^{20}, [(c)] W_t^{30}. Values are normalised so that the maximum SPL is at 0 dB.

around this region there is high pressure levels. However, since the two sources have the same total sound power, away from the region where the principal lobe of the dominant mode is incident, it is expected that $\Delta^{20}_{\text{source}}$ is mainly negative to compensate for the energy excess carried within the dominant mode.

In order to quantify the shielding effect, the metric Δ_{bl} is used as defined in section IV. This metric highlights the areas of shielding, and also gives insight into how the presence of a rotor-locked mode affects the shielding. Figure (12) demonstrates again the importance of refraction due to the boundary layer. As expected, the thicker the boundary layer the higher the amounts of shielding upstream. Moreover, it is very important to note that shielding does not seem to be affected by the presence of a dominant mode. Apart from minor differences in the principal lobe region, in the rest of the domain the two sources exhibit remarkably similar behavior. Even for the thickest boundary layer case, where any shielding effect is most pronounced, the presence of the dominant mode only causes minor differences in the region of

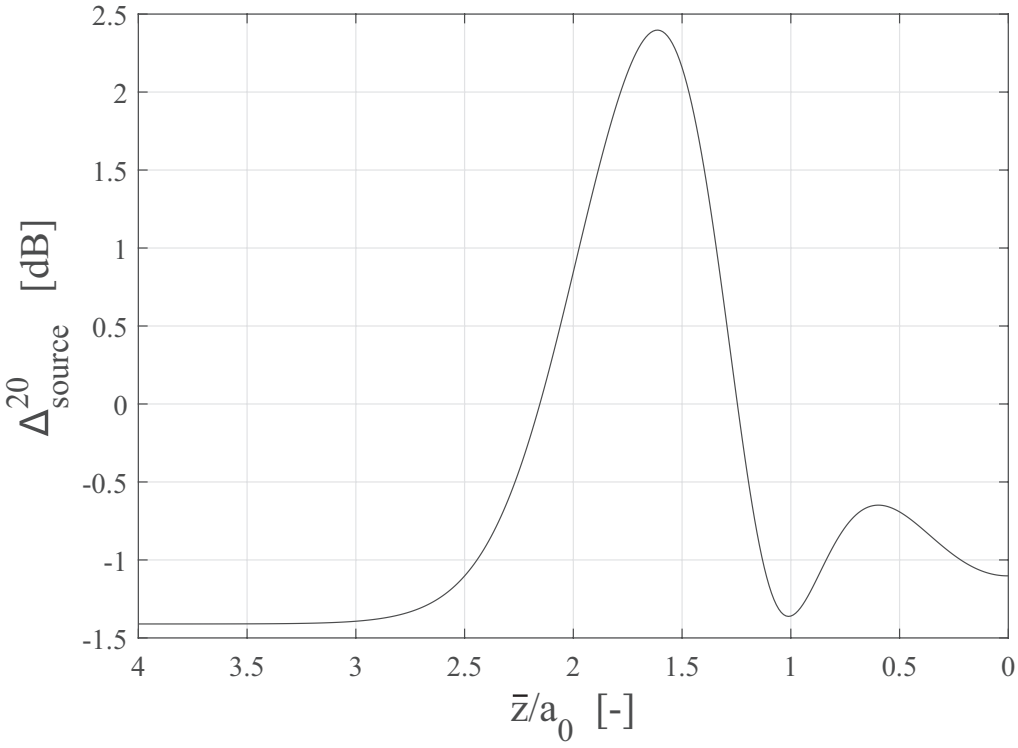

Fig. 11 $\Delta^{20}_{\text{source}}$ at $\bar{\phi} = 0$ for the average boundary-layer thickness.

the principal lobe. This result implies that it is not possible to manipulate shielding by manipulating the modal output of the engine.

Finally, the region very close to the plane of source ($\bar{z}/a_0 = 0$) should not be considered as accurate because in this region (90° to the duct's axis) the fuselage pressure levels are affected by diffraction around the lip of the duct, but this is not included in this analysis.

C. Comparison of Linear and Step-function Profiles

The results presented so far have been produced using an equivalent linear profile to approximate the 1/7th power-law profile. In this section some results generated using an equivalent step-function profile (eq.(21)) are presented, and compared with their equivalent that use a linear profile (eq.(30)). The contour maps shown in Fig. (13) show many similarities between the two approaches. Major discrepancies are observed in the shadow zone, however, as explained in section IV, differences there are largely irrelevant since the levels are very low and the accuracy is highly dependent on the numerical 'noise floor' of the prediction code. The pattern between the two contour maps is very similar, albeit the step-function exhibits more shielding further upstream. Results in Fig. (13) are for the average boundary-layer thickness which is 4.7% of the fuselage radius. This thickness value is expected to present discrepancies between the two approaches as is evident from Fig. (9).

Yet the major differences between the two approaches is seen to be predicted further upstream. This is also evident in Fig. (14) where for average and thick layers the further upstream the greater the difference between the shielding predictions with the two profiles. As expected, the discrepancy is much smaller in the case of the thin boundary layer. Ignoring the inaccurate results in the region very close to the plane of the source, $\bar{z}/a_0 < 1$, in the rest of the domain the two approaches are reasonably close to each other. Up to $\bar{z}/a_0 = 3$, for the average boundary-layer the difference between the predicted shielding with the two profiles is below 1 dB. This is also the case for the thick boundary- layer up to $\bar{z}/a_0 = 2.5$. It is reasonable to conclude that the predictions with the equivalent linear profile are less reliable further upstream as is evident from Fig. (9), in which case the step-function profile is more reliable. The further upstream sound propagates, the shallower the angle that it meets the boundary layer, meaning that the effective thickness of the

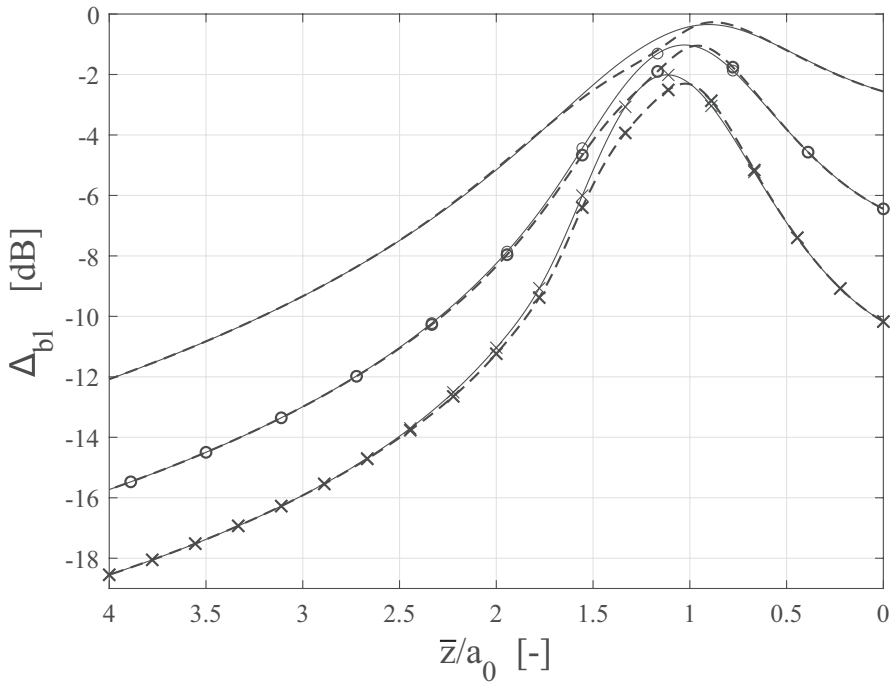

Fig. 12 Δ_{bl} **at** $\bar{\phi} = 0$ **for the three boundary-layer thicknesses and two sources,** W_t^{ee} **and** W_t^{20}**. Key:** W_t^{ee} **source with thin boundary-layer [solid line - no marker],** W_t^{ee} **source with average boundary-layer [solid line - ◯],** W_t^{ee} **source with thick boundary-layer [solid line - ×],** W_t^{20} **source with thin boundary-layer [dashed line - no marker],** W_t^{20} **source with average boundary-layer [dashed line - ◯],** W_t^{20} **source with thick boundary-layer [dashed line - ×].**

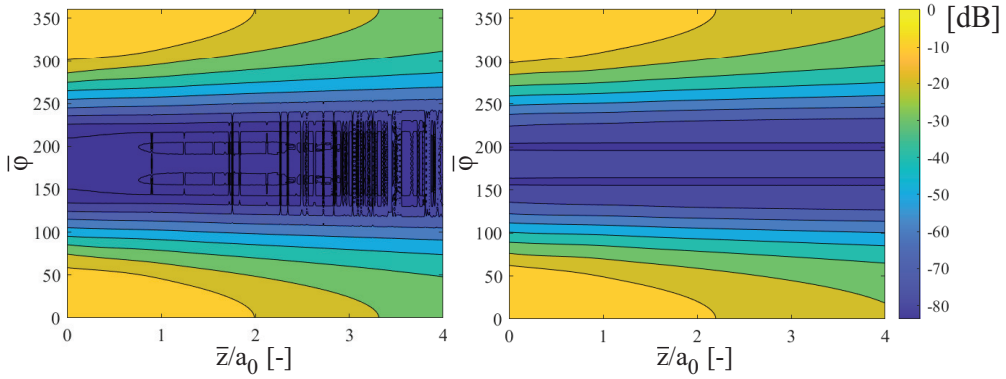

Fig. 13 SPL on the surface of the cylindrical fuselage for the average boundary-layer thickness and equal energy per mode source. [(left)] Equivalent step-function profile, [(right)] equivalent linear profile. Values are normalised so that the maximum SPL is at 0 dB.

layer is larger since the sound wave travels a greater distance to meet the fuselage at a shallower angle. This inevitably leads to a deterioration of the accuracy of the equivalent linear profile approach whose validity depends on the layer being sufficiently thin (see section III.C and Fig. (9)). However, for the axial range and boundary-layer thicknesses considered in the parametric study, the two approaches with the different velocity profiles show good agreement.

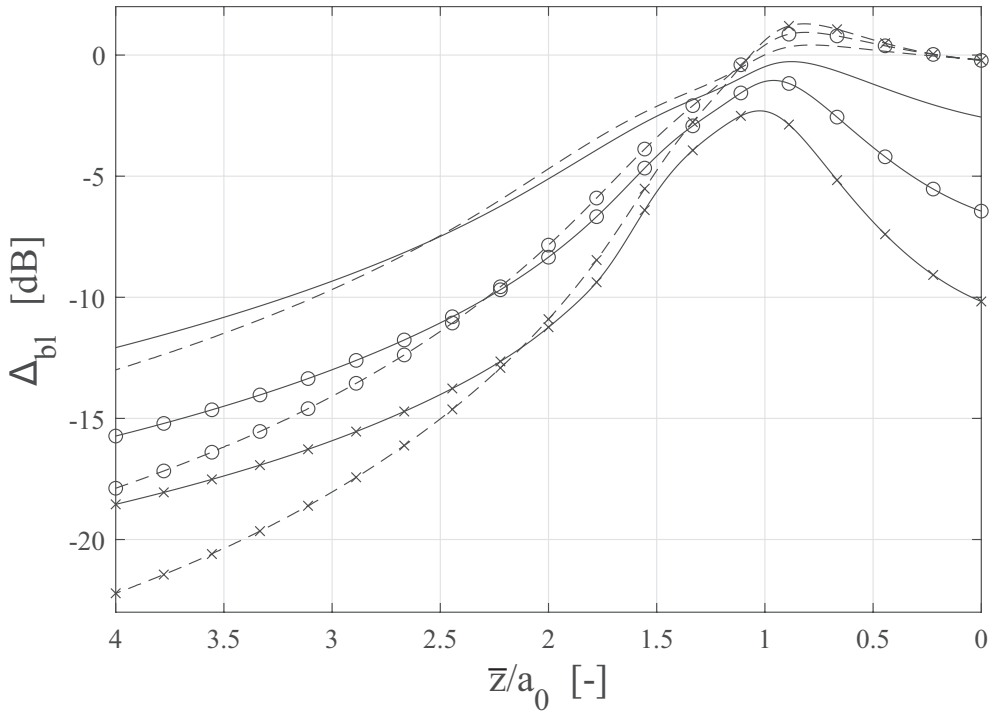

Fig. 14 Δ_{bl} **at** $\bar{\phi} = 0$ **for the three boundary-layer thicknesses and two equivalent profiles and** W_t^{20} **source. Key: Equivalent linear thin boundary-layer [solid line - no marker], equivalent linear with average boundary-layer [solid line - ◯], equivalent linear thick boundary-layer [solid line - ×], equivalent step-function thin boundary-layer [dashed line - no marker], equivalent step-function average boundary-layer [dashed line - ◯], equivalent step-function thick boundary-layer [dashed line - ×].**

D. Far-Field Polar Directivity

The results in this section are generated from the far-field eqs. (24) and (35). Far-field polar directivity plots are presented for the upstream area beneath the flight path, $0° < \bar{\theta} < 90°$, for the operating conditions discussed in V.A. Figure (15) shows the directivity for a thick boundary-layer using both equivalent linear and step-function velocity profiles. The source is the W_t^{20} as is evident by the presence of a distinctive lobe at about 55° which is very close to the group velocity modal propagation angle of the dominant mode (20,1). The rest of the directivity is much smoother which is consistent with a multi-modal source. As can be seen from Fig. (15), the predictions from the two different velocity profiles coincide, which supports the notion that in the far-field the type of fuselage boundary-layer profile used for the predictions does not matter, even for the thick layer case.

Figure (16) illustrates the effect of the boundary layer on the polar directivity. By comparing the predicted directivity patterns of the uniform flow case and the average boundary layer case, a phase shift is immediately apparent. The amplitude is unchanged as both far-field expressions (eqs. (14) and (35)) have an amplitude dependence proportional to $1/\bar{R}$, as expected. It is fair to conclude that the effect of the boundary layer on the far-field is not as pronounced as in the near-field. Despite this, the phase shift which is especially pronounced in the lobe area that exhibits the highest sound pressure levels, cannot be ignored.

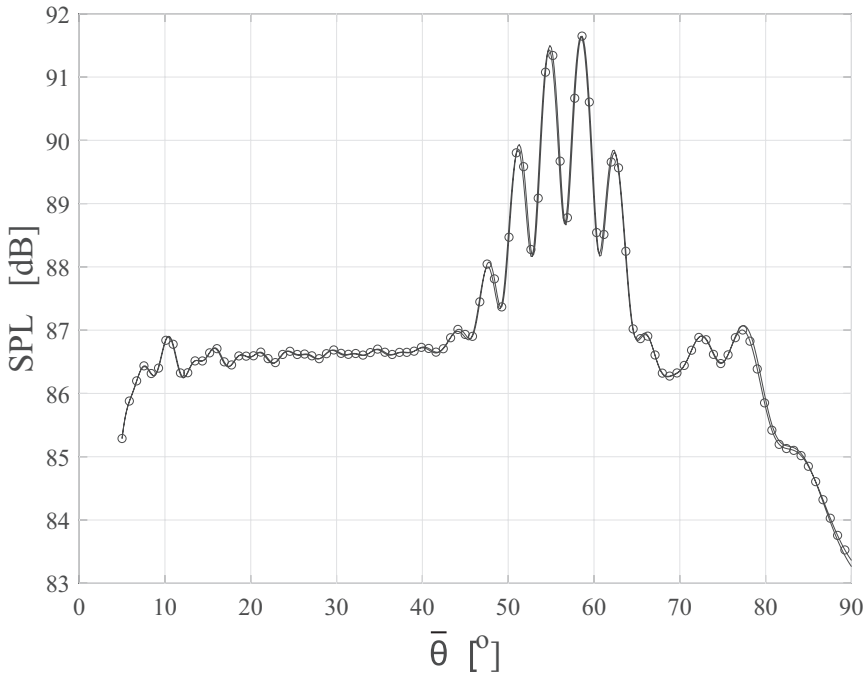

Fig. 15 Polar directivity of W_t^{20} source and thick boundary-layer using equivalent linear profile [solid line - no marker] and equivalent step-function profile [solid line - ○].

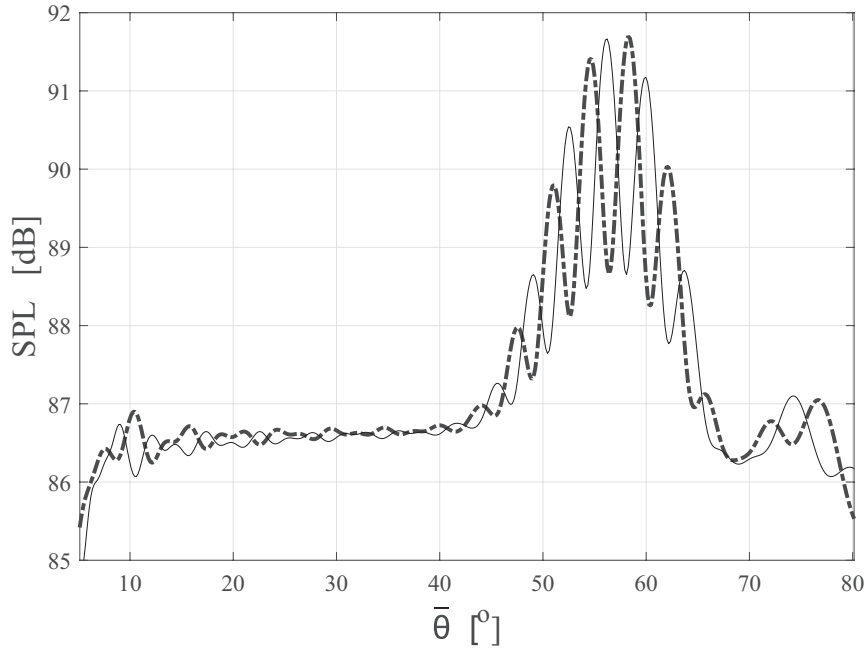

Fig. 16 Polar directivity of W_t^{20} source for average step-function boundary-layer [dashed line] and uniform flow [solid line].

VI. Summary

To summarise the work presented in this paper, two analytical-based models are presented that predict fan noise scattering by the fuselage, and the shielding effect owing to the presence of a boundary layer on the fuselage. The velocity profile is simplified by an equivalent linear or step-function profile with an effective thickness. This enables an analytical solution to the Pridmore-Brown equation (linear profile), or eliminates the need to solve this equation altogether (step-function profile). Therefore, both approaches avoid using time-consuming high-fidelity numerical schemes. The optimal method of matching the equivalent profiles to a power-law profile is investigated, and matching the shape factor proves to be the most effective.

Theoretical results produced using the two approaches are compared with existing numerical results, and reveal that both of them can effectively approximate the shielding effect of a realistic turbulent boundary-layer, modelled by a 1/7th power-law profile. The two approaches have their limitations regarding the thickness of the boundary layer, however they can still be used to produce fairly accurate and very quick predictions, giving valuable insight into the physics of the problem. Moreover, the accuracy of an equivalent step-function profile does not deteriorate with increasing thickness, making it an ideal candidate to use in parametric studies, as well as being the fastest method to compute because only the convected wave equation is solved.

Theoretical predictions are generated using the two approaches for a scenario based on a model aircraft operating in realistic flight conditions. Results from the multi-modal analysis show that the predictions of the fuselage surface pressure with either of the simplified model velocity profiles are in good agreement, suggesting that it may not be necessary to solve the Pridmore-Brown equation since the step-function results are comparable with those obtained solving with the linear shear. Moreover, the results of the multi-modal analysis suggest that the presence of a dominant rotor-locked mode does not affect the shielding, albeit its effect cannot be ignored on the total SPL on the fuselage surface. Finally, results for the far-field multi-modal analysis show minuscule differences between the predictions with either of the simplified model velocity profiles, but it is seen that modelling the refractive effect of the boundary layer for far-field simulations is necessary to ensure the correct phase of the lobes and nulls in the directivity, compared to simulations with uniform flow only.

Acknowledgments

The work in this article is part of the ARTEM project. This project has received funding from the European Union's Horizon 2020 research and innovation programme under grant No. 769 350. ARTEM and other projects within the MG1-2-2017 call 'Reducing Aviation Noise' were initiated by the EREA 'Future Sky' initiative. The first author also acknowledges the financial contribution from the EPSRC via the University of Southampton's Doctoral Training Grant. The authors wish to acknowledge the technical input to this work from Christoph Richter (Rolls–Royce plc). Also the authors wish to acknowledge the continuing support provided by Rolls–Royce plc through the University Technology Centre in Propulsion Systems Noise at the Institute of Sound and Vibration Research.

References

[1] International Civil Aviation Organisation, "Volume 1: Aircraft noise", *Annex 16 to the Convention on International Civil Aviation: Environmental Protection*, 5th edition, 2008.

[2] D.B. Hanson, "Shielding of prop-fan noise by the fuselage boundary layer", *Journal of Sound and Vibration*, **92**(4), pp. 591-598, 1984.

[3] D.B. Hanson and B. Magliozzi, "Propagation of propeller tone noise through a fuselage boundary layer", *Journal of Aircraft*, **22**(1), pp. 63-70, 1985.

[4] C.R. Fuller, "Free-field correction factor for spherical acoustic waves impinging on cylinders", *American Institute of Aeronautics and Astronautics Journal*, **27**(12), pp. 1722-1726, 1989.

[5] J. Gaffney, A. McAlpine, M.J. Kingan, "Fuselage boundary-layer refraction of fan tones radiated from an installed turbofan aero-engine", *Journal of Acoustical Society of America*, **141**(3), pp. 1653-1663, 2017.

[6] D-M. Rouvas and A. McAlpine,"Theoretical methods for the prediction of near-field and far-field sound radiation of fan tones scattered by a cylindrical fuselage", *Proceedings of the AIAA Aviation 2021 Forum*, AIAA-2021-2300, August 2–6, 30 pages, https://doi.org/10.2514/6.2021-2300.

[7] G.L. McAninch, "A note on propagation through a realistic boundary layer", *Journal of Sound and Vibration*, **88**(2), pp. 271-274, 1983.

[8] C.K.W. Tam and P.J. Morris, "The radiation of sound by the instability waves of a compressible plane turbulent shear layer", *Journal of Fluid Mechanics*, **98**(2), pp. 349-381, 1980.

[9] D. C. Pridmore-Brown,"Sound propagation in a fluid flowing through an attenuating duct", *Journal of Fluid Mechanics*, **4**, pp. 393-406, 1958.

[10] D-M. Rouvas and A. McAlpine,"Prediction of Fan Tone Radiation Scattered By a Cylindrical Fuselage", *Proceedings of the 11th EASN International Conference on Innovation in Aviation & Space to the satisfaction of the European Citizens*, 1–3 September 2021, doi:10.1088/1757-899X/1226/1/012050

[11] H.Y. Lu, "Fuselage Boundary-Layer Effects on Sound Propagation and Scattering", *American Institute of Aeronautics and Astronautics Journal*, **28**(7), pp. 1180-1186, 1990.

[12] I.V. Belyaev, "The Effect of an Aircraft's Boundary Layer on Propeller Noise", *Acoustical Physics*, **58**(4), pp. 425-433, 2012.

[13] H.H. Brouwer,"The Scattering of Open Rotor Tones by a Cylindrical Fuselage and its Boundary Layer", *Proceedings of the 22nd AIAA/CEAS Aeroacoustics Conference*, AIAA-2016-2741, May 30–June 1, 2016.

[14] W. Eversman and R.J. Beckemeyer,"Transmission of sound in ducts with thin shear layers-Convergence to the uniform flow case", *Journal of the Acoustical Society of America*, **52**(1), pp. 216-220, 1972.

[15] M. Goldstein and E. Rice,"Effect of shear on duct wall impedance", *Journal of Sound and Vibration*, **30**(1), pp. 79-84, 1973.

[16] A. McAlpine, J. Gaffney, M.J. Kingan, "Near-field sound radiation of fan tones from an installed turbofan aero-engine", *Journal of Acoustical Society of America*, **138**(3), pp. 1313-1324, 2015.

[17] J. Gaffney, *Theoretical Methods to Predict Near-field Fuselage Installation Effects due to Inlet Fan Tones*, Ph.D. thesis, University of Southampton, 2016.

[18] J.M. Tyler and T.G. Sofrin, "Axial flow compressor noise studies", *SAE Technical Paper*, **70**, pp. 309-332, 1962.

[19] M. Abramowitz and I. Stegun, *Handbook of Mathematical Functions*, Dover Publications, Inc., New York, 1965. (Chapter 9, pp. 363)

[20] Bowman, J.J. Senior, T.B.A. and Uslenghi, P.L.E, *Electromagnetic and Acoustic Scattering by Simple Shapes*, North-Holland Publishing Co., 1969.

[21] S. Mariano,"Effect of wall shear layers on the sound attenuation in acoustically lined rectangular ducts", *Journal of Sound and Vibration*, **19**(3), pp. 261-275, 1971.

[22] S.-H. Ko,"Sound attenuation in acoustically lined circular ducts in the presence of uniform flow and shear flow", *Journal of Sound and Vibration*, **22**(2), pp. 193-210, 1972.

[23] P.G.J. Schwaller, N.J. Baker, J.D. Tomlinson, P Sijitsma,"Noise Validation of Model Fan Rig with Engine", *Proceedings of the 12th AIAA/CEAS Aeroacoustics Conference*, AIAA-2006-2479, May 8-10, 2006.

[24] I. Achunche, J. Astley, R. Sugimoto, A. Kempton,"Prediction of Forward Fan Noise Propagation and Radiation from Intakes", *Proceedings of the 15th AIAA/CEAS Aeroacoustics Conference*, AIAA-2009-3239, May 11-13, 2009.